Inorganic Chemistry
Cite This: Inorg. Chem. 2018, 57, 12740−12755
Article
pubs.acs.org/IC

# Slow Magnetic Relaxation in Cobalt(II) Field-Induced Single-Ion Magnets with Positive Large Anisotropy

Anna Świtlicka,*[,†] Barbara Machura,[†] Mateusz Penkala,[‡] Alina Bieńko,*[,§] Dariusz C. Bieńko,[∥] Ján Titiš,[⊥] Cyril Rajnák,[⊥] Roman Boča,[⊥] Andrew Ozarowski,[#] and Mykhaylo Ozerov[#]

[†]Department of Crystallography, Institute of Chemistry and [‡]Department of Organic Synthesis, Institute of Chemistry, University of Silesia, Szkolna Street 9, 40-006 Katowice, Poland

[§]Faculty of Chemistry, University of Wroclaw, Joliot-Curie 14, 50-383 Wroclaw, Poland

[∥]Faculty of Chemistry, Wroclaw University of Technology, Wybrzeze Wyspiańskiego 27, 50-370 Wroclaw, Poland

[⊥]Department of Chemistry, Faculty of Natural Sciences, University of SS Cyril and Methodius, 917 01 Trnava, Slovakia

[#]National High Magnetic Field Laboratory, Florida State University, 1800 East Paul Dirac Drive, Tallahassee, Florida 32310, United States

Supporting Information

**ABSTRACT:** Three pentacoordinate complexes of the type $[Co(pypz)X_2]$, where *pypz* is a tridentate ligand 2,6-bis(pyrazol-1-yl)pyridine and X = $Cl^-$ (**1**), $NCS^-$ (**2**), and $NCO^-$ (**3**), have been synthesized, and their structures have been determined by X-ray analysis. The DC magnetic data show a sizable magnetic anisotropy, which was confirmed by high-field high-frequency electron paramagnetic resonance (HF EPR) measurements. Well-resolved HF EPR spectra of high spin cobalt (II) were observed over the microwave frequency range 100−650 GHz. The experimental spectra of both complexes were simulated with axial *g* tensor components, a very large positive *D* value, and different *E*/*D* ratios. To determine the exact *D* value for **2** (38.4 $cm^{-1}$) and **3** (40.92 $cm^{-1}$), the far-infrared magnetic spectroscopy method was used. Knowledge of the zero field splitting parameters and their signs is crucial in interpreting the single-molecule magnet or single chain magnet behavior. The AC susceptibility data confirm that these complexes exhibit a slow magnetic relaxation under small applied DC field with two (**1** and **3**) or three (**2**) relaxation modes.

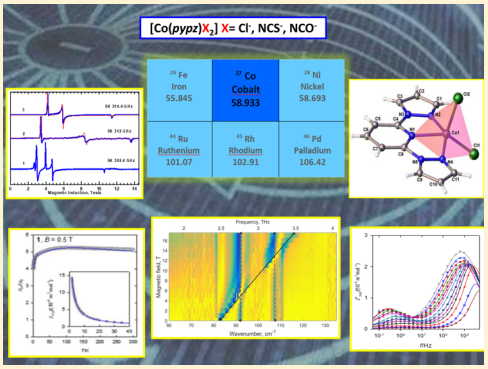


## INTRODUCTION

Slow magnetic relaxation in multinuclear coordination clusters and low-coordinate transition metal complexes have achieved enormous interest during the past few decades, and they have become one of the most attractive subjects in inorganic chemistry and materials science. The motivation for these studies lies in the area of potential applications such as switches, sensors, displays, and high-density information storage devices.[1−11] Until 2003, the scientists' efforts have been predominately focused on the synthesis of molecular clusters with the highest possible ground-state spin and negative axial magnetic anisotropy and understanding the unique magnetic properties of these systems.[12−18] The first observation of hysteresis and quantum tunneling of the magnetization in mononuclear double-decker bis(phthalocyaninato)terbium(III) and dysprosium(III) constituted the development of a novel class of compounds, referred to as single-ion magnets (SIMs) by analogy to single-molecule magnets (SMMs).[19] While SMMs are constructed from a number of strongly magnetically coupled anisotropic metal centers, SIM behavior depends on the magnetic properties of a single paramagnetic ion in the ligand field.[20−24] Another approach to develop new attractive magnetic materials concerns using SIM building blocks to assemble them into one-, two-, and three-dimensional metal−organic frameworks.[25−30] The slow magnetic relaxation of magnetization was confirmed also for the coordination polymers with paramagnetic metal centers (Co(II)) separated through neutral or anionic spacers such as 1,3-bis(4-pyridyl)azulene,[31] 4,4′-bipyridine,[32] or dicyanoamide ions.[33,34]

Among 3d metal ions, the cobalt(II) atom is a suitable candidate for synthesis of SIMs due to its high magnetic anisotropy and strong first order spin-orbit coupling displayed by the metal in the +II oxidation state.[22] SIMs species with Co(II) ions are complexes with coordination numbers between 2 and 8. It has been evidenced that low coordination numbers minimize the ligand field relative to the spin−orbit coupling, enhancing the magnetic anisotropy.[21,22,35−37] Interestingly, magnetic properties of $[Co(terpy)Cl_2]$, $[Co(terpy)(NCS)_2]$, and $[Co(terpy)_2](NCS)_2 \cdot 1.5H_2O$ were shown to be controlled by a number of coordinated *terpy* molecules as well as a kind of

Received: July 12, 2018
Published: October 2, 2018







DOI: 10.1021/acs.inorgchem.8b01906
Inorg. Chem. 2018, 57, 12740−12755

anionic ligands. While $[Co(terpy)_2](NCS)_2 \cdot 1.5H_2O$ exhibited a thermally induced spin crossover behavior of the $[Co(terpy)_2]^{2+}$ unit from a high spin ($S = 3/2$) at higher temperatures to a low-spin ($S = 1/2$), two different relaxation processes—fast and slow—were observed for compounds $[Co(terpy)Cl_2]$ and $[Co(terpy)(NCS)_2]$, with barriers to spin reversal (fast/slow) of 19.5/2.8 $cm^{-1}$ and 11.8/2.1 $cm^{-1}$, respectively. It was theoretically demonstrated that the first excited Kramers doublet of $[Co(terpy)Cl_2]$ is approximately twice as high in energy compared to $[Co(terpy)(NCS)_2]$. Replacement of chlorido ligands by $NCS^-$ ions leads to a decrease in the energy barrier.[38]

Rational control in the synthesis of cobalt(II) complexes of a desired magnetic behavior, however, still remains a great challenge, and much more work is required to extend our knowledge of the structure—property relationship. The current research concerns the preparation, structural characterization, and variable-temperature magnetic and high-frequency electron paramagnetic resonance (HF EPR) studies of the cobalt(II) complexes with 2,6-bis(pyrazol-1-yl)pyridine (Scheme 1), developed as a structural analogue of 2,2′:6′,2″-terpyridine, and the main research objective was to investigate the role of chlorido or pseudohalido ligands in controlling the geometry and magnetic behavior of $[Co(pypz)Cl_2]$ (**1**), $[Co(pypz)(NCS)_2]$ (**2**), and $[Co(pypz)(NCO)_2]$ (**3**). In contrast to the vast coordination chemistry of 2,2′:6′,2″-terpyridines,[39] the number of the related transition metal complexes $[Co(pypz)Cl_2]$ is very limited.[40−43]

**Scheme 1. Ligand 2,6-Bis(pyrazol-1-yl)pyridine (*pypz*)**

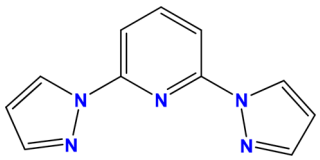

## EXPERIMENTAL SECTION

**Materials and General Methods.** 2,6-Bis(pyrazol-1-yl)pyridine (*pypz*) was synthesized according to the literature method.[44] The other reagents were commercially available, and they were used without further purification. Elemental analyses (C, H, N) were performed on Perkin—Elmer Series II and Vario EL III analyzers. IR spectra were recorded on a Nicolet iS5 Fourier transform infrared (FT-IR) spectrophotometer in the spectral range 4000−400 $cm^{-1}$ with the samples in the form of KBr pellets. The electronic spectra were obtained from solid state samples on Nicolet Evolution 220 (190−1100 nm) and Nicolet iS50 FT-IR (700−1500 nm) spectrophotometers.

*Synthesis of [Co(pypz)Cl$_2$], (1).* $CoCl_2 \cdot 6H_2O$ (0.10 g, 0.42 mmol) dissolved in water (25 $cm^3$) was slowly added to a methanolic solution of ligand *pypz* (0.09 g, 0.42 mmol). The resulting solution was continuously stirring for 15 min, and then the mother liquor was left to slow evaporation at room temperature. X-ray quality blue prisms of **1** were formed after a few days. They were collected by filtration and dried in the open air. Yield ca. 60%. IR (KBr/$cm^{-1}$): 1478(s), 1402(m), 1345(m) [$\nu$(C = N)$_{pypz}$ and $\nu$(C = C)$_{pypz}$]; Anal. Calc. for $C_{11}H_9Cl_2N_5Co$ (**1**): C, 38.73; H, 2.66; N, 20.53%. Found: C, 38.72; H, 2.95, N 20.47%.

*Synthesis of [Co(pypz)(NCS)$_2$], (2).* $NH_4NCS$ (0.05 g, 0.65 mmol) and $CoCl_2 \cdot 6H_2O$ (0.10 g, 0.42 mmol) dissolved in water (25 $cm^3$) were slowly added to a methanolic solution of ligand *pypz* (0.09 g, 0.42 mmol). The resulting solution was continuously stirring for 15 min, and then the mother liquor was left to slow evaporation at room temperature. X-ray quality blue prisms of **2** were formed after a few days. They were collected by filtration and dried in the open air. Yield ca. 70%. IR (KBr/$cm^{-1}$): 2079(vs) [$\nu$(C = N$_{SCN}$)], 1480(s), 1401(m), 1343(m) [$\nu$(C═N)$_{pypz}$ and $\nu$(C═C)$_{pypz}$]; Anal. Calc. for $C_{13}H_9N_7S_2Co$ (**2**): C, 40.31; H, 2.60; N, 25.31%. Found: C, 40.25; H, 2.49, N 24.69%.

*Synthesis of [Co(pypz)(NCO)$_2$], (3).* The same synthetic procedure as that for **3** was used, except that ammonium thiocyanate was replaced with sodium cyanate (0.055 g, 0.84 mmol). X-ray quality blue prisms of **3** were formed after a few days. They were collected by filtration and dried in the open air. Yield ca. 65%. IR (KBr/$cm^{-1}$): 2212(s) [$\nu_{as}$(C≡N)$_{NCO}$], 1482(m), 1405(m), 1345(s) [$\nu$(C═N)$_{pypz}$ and $\nu$(C═C)$_{pypz}$]; Anal. Calc. for $C_{13}H_9N_7O_2Co$ (**3**): C, 43.96; H, 2.84; N, 27.60%. Found: C, 43.89; H, 2.69, N 27.50%.

**Magnetic Measurements.** Variable-temperature (2−300 K) direct current (DC) magnetic susceptibility measurements under applied field $B_{DC}$ = 0.1 T (below 20 K) and 1.0 T (above 20 K) and variable-field (0−7 T) magnetization measurements at low temperatures in the range 2−7 K were carried out with Quantum Design SQUID magnetometer. Variable-temperature (2 − 8 K) alternating current (AC) magnetic susceptibility measurements under different applied static fields in the range of $B_{DC}$ = 0−0.5 T were carried out with Quantum Design Physical Property Measurement System (PPMS). Raw magnetic susceptibility data were corrected for the underlying diamagnetism and the sample holder. Magnetic measurements were carried out by crushing the crystals and restraining the sample in order to prevent any displacement due to its magnetic anisotropy.

**EPR and Far-Infrared Magnetic Spectroscopy (FIRM) Studies.** Far-infrared magnetic spectroscopy was performed at the National High Magnetic Field Laboratory on a 17 T vertical-bore superconducting magnet using a Fourier-transform infrared spectrometer Bruker Vertex 80v. The evacuated (∼4 mBar) optical beamline was used for their coupling, and the experimental setup was equipped by a mercury lamp and a composite silicon bolometer (Infrared Laboratories), as a THz radiation source and detector, respectively. Eicosane pellets containing the studied compound were measured in the spectral region between 18 and 730 $cm^{-1}$ (0.55−22 THz) with the resolution of 0.3 $cm^{-1}$ (9 GHz). Both sample and bolometer were cooled by a low-pressure helium gas to the temperature of 4.6 K. Transmittance spectra were calculated as the THz intensity spectrum at each magnetic field divided by the THz intensity spectrum averaged for all fields.

**Crystal Structure Determination and Refinement.** Single crystal X-ray diffraction data of **1**−**3** were collected on a Gemini A Ultra diffractometer equipped with Atlas CCD detector and graphite monochromated MoK$\alpha$ radiation ($\lambda$ = 0.71073 Å) at room temperature. The unit cell determination and data integration were carried out using the CrysAlis package of Oxford Diffraction.[45] Lorentz, polarization, and empirical absorption correction using spherical harmonics implemented in SCALE3 ABSPACK scaling algorithm were applied.[46] The structures were solved by the direct methods using SHELXS97 and refined by full-matrix least-squares on $F^2$ using SHELXL97.[47] All non-hydrogen atoms were refined anisotropically. The hydrogen atoms were placed in calculated positions refined using idealized geometries (riding model) and assigned fixed isotropic displacement parameters, $d$(C−H) = 0.93 Å, $U_{iso}$(H) = 1.2 $U_{eq}$(C) (for aromatic); and $d$(C−H) = 0.96 Å, $U_{iso}$(H) = 1.5 $U_{eq}$(C) (for methyl). The methyl groups were allowed to rotate about their local 3-fold axis. Details of the crystallographic data collection, structural determination, and refinement for **1**−**3** are given in Table 1, whereas selected bond distances and angles are listed in Table S1.

## RESULTS AND DISCUSSION

**Structural Description of 1, 2, and 3.** Perspective views of the molecular structures of **1**, **2**, and **3** together with the atom numbering are depicted in Figure 1a. The molecule $[Co(pypz)(NCO)_2]$ has crystallographically imposed 2-fold



DOI: 10.1021/acs.inorgchem.8b01906
Inorg. Chem. 2018, 57, 12740−12755

**Table 1. Crystal Data and Structure Refinement for 1−3**

| | 1 | 2 | 3 |
|---|---|---|---|
| empirical formula | $C_{11}H_9Cl_2N_5Co$ | $C_{13}H_9N_7S_2Co$ | $C_{13}H_9N_7O_2Co$ |
| formula weight | 341.06 | 386.32 | 354.20 |
| temperature [K] | 293.0(2) | 293.0(2) | 293.0(2) |
| wavelength [Å] | 0.71073 | 0.71073 | 0.71073 |
| crystal system | monoclinic | triclinic | monoclinic |
| space group | $P2_1/c$ | $P\bar{1}$ | $C2/c$ |
| unit cell dimensions [Å, °] | $a$ = 10.8105(10) | $a$ = 8.1959(6) | $a$ = 13.2040(16) |
| | $b$ = 8.0190(6) | $b$ = 8.3196(5) | $b$ = 9.1619(6) |
| | $c$ = 15.1517(11) | $c$ = 13.7359(12) | $c$ = 12.6555(16) |
| | | $\alpha$ = 93.374(6) | |
| | $\beta$ = 94.384(7) | $\beta$ = 103.702(7) | $\beta$ = 112.237(14) |
| | | $\gamma$ = 114.555(7) | |
| volume [Å$^3$] | 1309.65(18) | 814.44(12) | 1417.1(3) |
| $Z$ | 4 | 2 | 4 |
| density (calculated) [g cm$^{-3}$] | 1.730 | 1.575 | 1.660 |
| absorption coefficient [mm$^{-1}$] | 1.709 | 1.318 | 1.233 |
| $F$(000) | 684 | 390 | 716 |
| crystal size [mm] | 0.33 × 0.10 × 0.04 | 0.24 × 0.07 × 0.06 | 0.27 × 0.26 × 0.07 |
| $\theta$ range for data collection [°] | 3.38 to 25.05 | 3.38 to 25.05 | 3.33 to 25.05 |
| index ranges | $-11 \le h \le 12$ | $-9 \le h \le 8$ | $-15 \le h \le 14$ |
| | $-9 \le k \le 9$ | $-9 \le k \le 9$ | $-10 \le k \le 9$ |
| | $-18 \le l \le 17$ | $-16 \le l \le 14$ | $-15 \le l \le 14$ |
| reflections collected | 6164 | 5897 | 3167 |
| independent reflections | 2310 ($R_{int}$ = 0.0662) | 2874 ($R_{int}$ = 0.0391) | 1247 ($R_{int}$ = 0.0360) |
| completeness to 2$\theta$ [%] | 99.7 | 99.7 | 98.9 |
| max and min transmission | 1.00 and 0.044 | 1.00 and 0.479 | 1.00 and 0.675 |
| data/restraints/parameters | 2310/0/172 | 2874/0/208 | 1247/0/107 |
| goodness-of-fit on $F^2$ | 1.137 | 1.034 | 1.075 |
| final $R$ indices [$I > 2\sigma(I)$] | $R1$ = 0.0381 | $R1$ = 0.0546 | $R1$ = 0.0366 |
| | $wR2$ = 0.0802 | $wR2$ = 0.1208 | $wR2$ = 0.0824 |
| $R$ indices (all data) | $R1$ = 0.0656 | $R1$ = 0.0858 | $R1$ = 0.0449 |
| | $wR2$ = 0.1012 | $wR2$ = 0.1307 | $wR2$ = 0.0867 |
| largest diff peak and hole [e·Å$^{-3}$] | 0.464 and −0.454 | 0.578 and −0.330 | 0.315 and −0.354 |
| CCDC deposit number | 1831189 | 1831188 | 1831190 |

symmetry; the Co(II) ion, nitrogen (N1), and carbon (C6) atoms are located on a 2-fold crystallographic axis. The Co−N bond of the central pyridyl ring of *pypz* ligand of **1**, **2**, and **3** [Co(1)−N(1) = 2.085(3) Å in **1**, Co(1)−N(1) = 2.057(3) Å in **2**, and Co(1)−N(1) = 2.069(3) Å in **3**] are shorter than those of the outer pyrazol-1-yl rings [Co(1)−N(2) = 2.169(4) Å; Co(1)−N(4) = 2.145(4) Å in **1**; Co(1)−N(2) = 2.176(4) Å; Co(1)−N(4) = 2.120(4) Å in **2** and Co(1)−N(2) = 2.216(3) Å; Co(1)−N(2)b = 2.216(3) Å in **3**], while all Co−$N_{pypz}$ bond lengths are longer than the Co−Cl [Co(1)−Cl(1) = 2.2816(13) Å; Co(1)−Cl(2) = 2.2964(14) Å] and Co−$N_{NCX}$ distances [Co(1)−N(98) = 1.962(4) Å; Co(1)−N(99) = 1.944(4) Å in **2** and Co(1)−N(99) = 1.986(3) Å; Co(1)−N(99)b = 1.986(3) Å in **3**]. The ligands $NCX^-$ are quasi-linear with the values of the N−C−X angle of 179.7(5)° and 178.6(5)° in **2** and 178.4(3)° in **3**. Slight bending is observed at the nitrogen atom of the thiocyanate/cyanate group [(C(98)−N(98)−Co(1) = 162.0(4)°; C(99)−N(99)−Co(1) = 171.7(4)° in **2** and (C(99)−N(99)−Co(1) = 160.4(2)° in **3**].

In all these complexes, the cobalt center is penta-coordinated by the three N donor atoms of the *pypz* ligand and two N atoms of the terminal $Cl^-$ (**1**) or $NCX^-$ ligands ($NCS^-$ in **2** and $NCO^-$ in **3**). Halido and pseudohalido ligands have a significant impact on the geometry of the metal coordination sphere. The angular structural index parameter $\tau$,[48] called also the Addison parameter, expresses the difference between the two largest angles divided by 60, and it equals 0.10 for **1**, 0.36 for **2**, and 0.46 for **3**. Compared to the ideal values of $\tau$ = 1 for an trigonal bipyramid and $\tau$ = 0 for a square pyramid, the $\tau$ values for **2** and **3** indicate an intermediate geometry between square pyramid and trigonal bipyramid stereochemistry, although much closer to the former in the case of **2**. The displacement of the cobalt atom from the trigonal plane formed by two pseudohalido and pyridyl nitrogen atoms and tetragonal plane defined by *pypz*-N donors and one nitrogen atom of $NCX^-$ group are 0.130 Å and 0.567 Å in **2** and 0.023 Å and 0.556 Å in **3**, respectively. Complex **1** was found to be best described as a distorted square pyramid. The cobalt atom deviates by 0.556 Å from the least-squares basal plane defined by three nitrogen atoms of *pypz* and Cl(1) atom.

The crystal packing analysis (Mercury 2.4 program)[49] demonstrates that the molecules [Co(*pypz*)$X_2$] (X = $Cl^-$, $NCS^-$, or $NCO^-$) are arranged in an alternate head-to-tail manner through $\pi-\pi$ stacking interactions, forming supramolecular chains (Figure 1b). In the crystal structure of compound **3**, the chains are additionally stabilized by hydrogen bonds, forming a supramolecular 2D network (C(1)−H(1)···O(99)$^d$ [D···A distance = 3.285(4) Å and D−H···A angle =



DOI: 10.1021/acs.inorgchem.8b01906
*Inorg. Chem.* 2018, 57, 12740−12755

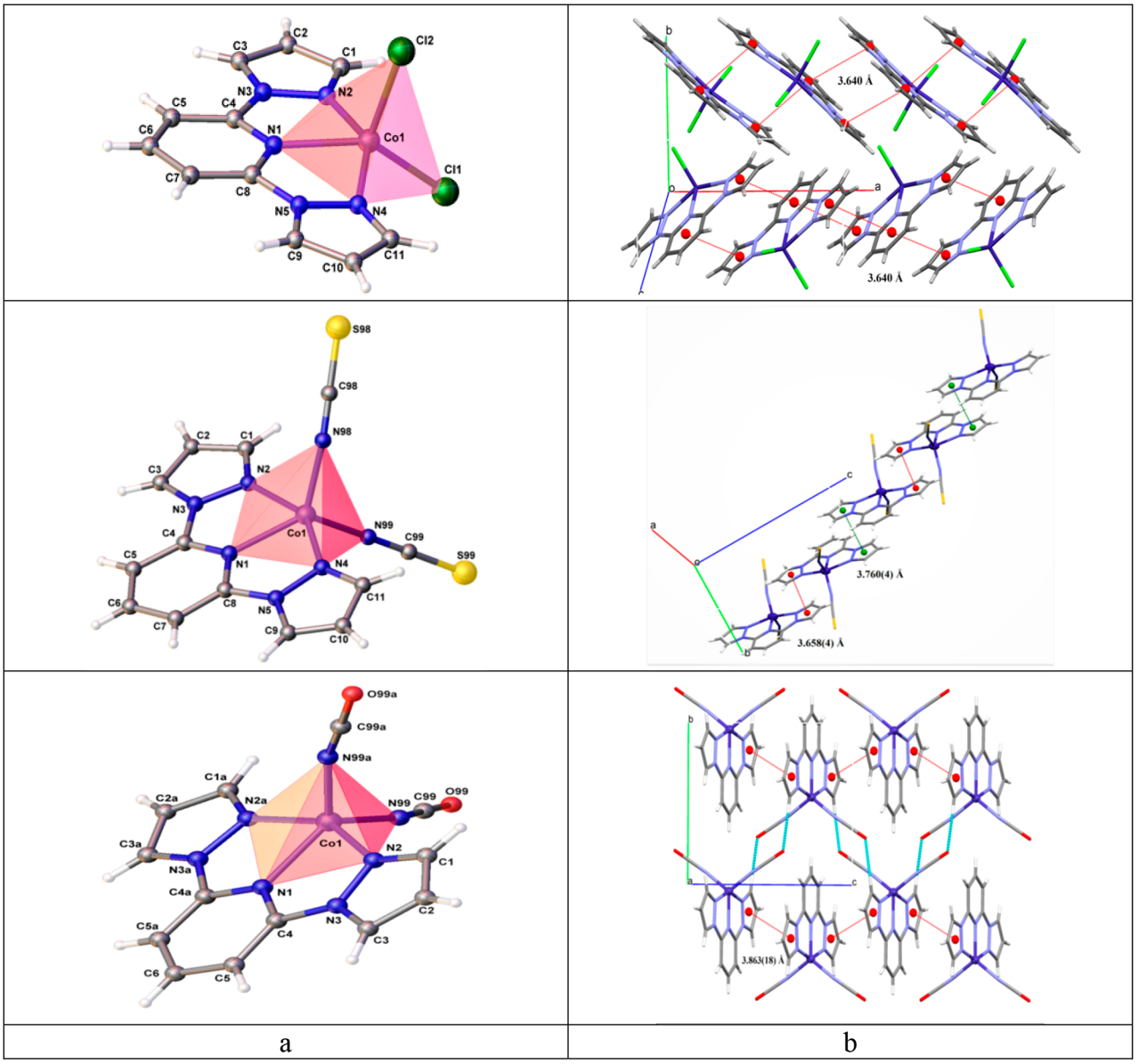


**Figure 1.** (a) Perspective views of the molecular structures of $[Co(pypz)Cl_2]$ (**1**), $[Co(pypz)(NCS)_2]$ (**2**), and $[Co(pypz)(NCO)_2]$ (**3**) together with the atom numbering; displacement ellipsoids are drawn at the 50% probability level [symmetry codes: (a): $1 - x, y, 1/2 - z$]; (b) view of the supramolecular chain generated via $\pi-\pi$-stacking interactions in compounds **1** and **2** and the supramolecular 2D network generated by $\pi-\pi$-stacking interactions and hydrogen bonding in compound **3**.

170.0°; (d): $1/2 - x, 3/2 - y, -z$]. The shortest Co···Co separations within the chain are 6.164(1) in **1**, 7.674(2) Å in **2**, and 7.388(1) Å in **3.**

The coordination geometries of **1**−**3** have been further investigated by the continuous symmetry measures methodology,[50−54] which provides a quantitative measurement about the deviation of a given coordination sphere from the ideal geometry. The complexes **1**−**3** were compared to two ideal five-coordinate geometries, trigonal bipyramidal (TBY, $D_{3h}$ symmetry) and square pyramidal (SPY, $C_{4v}$ symmetry). The shape value ($S_Q$(P)) with respect to the square-pyramid geometry was found as 2.084 for **1**, 4.063 for **2**, and 5.973 for **3**, while the calculated distances to the ideal trigonal bipyramid are following: 4.140 for **1**, 3.071 for **3**, and 4.006 for **3**. According to the continuous symmetry measures (CSM) methodology, the shape measure $S_Q(P)$ is defined as

$$S_Q(P) = \min\left[\left(\sum_{i=1}^{n} |\vec{q}_i - \vec{p}_i|^2\right) / \left(\sum_{i=1}^{n} |\vec{q}_i - \vec{q}_0|^2\right)\right] \times 100 \quad (1)$$

Here, $\vec{q}_i$ are $N$ vectors that contain the $3N$ Cartesian coordinates of the problem structure Q; $\vec{p}_i$ contains the coordinates of the ideal polyhedron P; $\vec{q}_0$ is the position vector of the geometric center that is chosen to be the same for the two polyhedra. This parameter indicates minor distortions from the reference shape when it is less than 1. Values of up to 3 units indicate important distortions, but the reference shape provides still a good stereochemical description. Severely distorted chemical structures are characterized by greater values $S_Q(P)$.[50−53]

As indicated by the shape values, **2** is roughly equidistant in the shape continuum from trigonal bipyramidal and square



DOI: 10.1021/acs.inorgchem.8b01906
Inorg. Chem. 2018, 57, 12740−12755

Table 2. Calculated Energy Levels and Magnetic Parameters for 1 through 3[a]

| | 1 | 2 | 3 | [1] | [2] | [3] | [4] | [5] |
|---|---|---|---|---|---|---|---|---|
| idealized geometry | 4py | 3bpy | 3bpy | 4py | 4py | 3bpy | 3bpy | 4py |
| $\tau$ | 0.10 | 0.36 | 0.46 | 0.15 | 0.01 | 0.35 | 0.41 | 0.19 |
| | | | Ab Initio Calculations | | | | | |
| ground term | $^4E$ $C_{4v}$ | $^4A_2$" $D_{3h}$ | $^4A_2$" $D_{3h}$ | $^4E$ $C_{4v}$ | $^4E$ $C_{4v}$ | $^4A_2$" $D_{3h}$ | $^4A_2$" $D_{3h}$ | $^4E$ $C_{4v}$ |
| CASSCF + NEVPT2 energies of terms/cm$^{-1}$ | 0, | 0, | 0, | | | | | |
| | 717, $\Delta_1$ | 2840, | 3099, | | | | | |
| | 2219, $\Delta_2$ | 3391 | 3138 | | | | | |
| six lowest Kramers doublets | 0, | 0, | 0, | 0, | 0, | 0, | 0, | 0, |
| (spin−orbit corrected levels)/cm$^{-1}$ | 172, $\delta_1$ | 76, | 86 ∼ 2$D$, | 137, | 243, | 91, | 88, | 121, |
| | 799, | 2531, | 2540, | 1125, | 574, | 1761, | 1860, | 1033, |
| | 1068, | 2900, | 3019, | 1374, | 879, | 2191, | 2313, | 1200, |
| | 2457, | 3548, | 3466, | 2663, | 2626, | 2796, | 2880, | 3098, |
| | 2504 | 3787 | 3799 | 2709 | 2693 | 3154 | 3286 | 3189 |
| $g_1$, $g_2$, $g_3$ | 1.929, | 2.018, | 2.001, | 1.97, | 1.74, | 1.99, | 1.99, | 2.06, |
| | 2.263, | 2.312, | 2.362, | 2.33, | 1.96, | 2.37, | 2.39, | 2.32, |
| | 2.968 | 2.421 | 2.474 | 2.82 | 3.29 | 2.50 | 2.47 | 2.89 |
| $(D/hc)$/cm$^{-1}$[b] | (−81.1) | 37.0 | 42.3 | (−61.6) | (−119) | 44.2 | 43.4 | (−58.1) |
| $E/D$ | 0.21 | 0.13 | 0.13 | 0.28 | 0.11 | 0.14 | 0.10 | 0.17 |
| | | | DC Magnetic Data | | | | | |
| ZFS model[c] | inappropriate | fails | m, zfs | m, zfs | d, zfs | d, zfs | m, zfs | d, zfs |
| $g_z$ | | [2.0] | [2.0] | [2.0] | [2.0] | [2.0] | [2.0] | [2.0] |
| $g_x$ | | 2.98(1) | 2.65(3) | 2.48 | 3.03 | 2.72 | 2.35 | 3.05 |
| $(D/hc)$/cm$^{-1}$ | | 48(13) | 30(16) | 61.9 | 153 | 70.1 | 46.8 | 87.5 |
| $(J/hc)$/cm$^{-1}$ | | | | | +1.45 | +1.42 | | +1.06 |
| $(zj/hc)$/cm$^{-1}$ | | −0.006 | −0.020 | −0.059 | | | −0.026 | |
| $\chi_{TIM}$/10$^{-9}$ m$^3$mol$^{-1}$ | | −43 | −5 | 2.5 | −53 | −18 | 9 | −54 |
| GFL model[c] | m, GF | m, GF | fails | | | | | |
| $(A\kappa\lambda/hc)$/cm$^{-1}$ | −181(8) | −124(13) | | | | | | |
| $(\Delta_{ax}/hc)$/cm$^{-1}$ | [−4000] | [−8000] | | | | | | |
| $g_L$ | −1.94(1) | −1.56(2) | | | | | | |
| $(zj/hc)$/cm$^{-1}$ | −0.073(1) | −0.033(3) | | | | | | |
| $\chi_{TIM}$/10$^{-9}$ m$^3$mol$^{-1}$ | −5(1) | −5(3) | | | | | | |
| | | | EPR Data | | | | | |
| $g_z$ | | 2.0 | 2.0 | | | | | |
| $g_x$ | | 2.18 | 2.175 | | | | | |
| $g_y$ | | 2.46 | 2.43 | | | | | |
| $(D/hc)$/cm$^{-1}$ | | 38.4 | 40.92 | | | | | |
| $(E/hc)$/cm$^{-1}$ | | 9.8 | 3.18 | | | | | |

[a]SPY = 4py = tetragonal (square) pyramid; TBY = 3bpy = trigonal bipyramid. Complexes studied previously: [1] − $[CoCl_2L^{C0}]_2$, [2] − $[CoCl_2L^{C7}]_2$, [3] − $[CoCl_2L^{C10}]_\infty$, [4] − $[CoCl_2L^{C12}]_\infty$, [5] − $[CoCl_2L^{C14}]_2$ with *para*-substituted pyridine ring by alkyl chain.[81] [b]Values in parentheses are meaningless owing to the quasi-degeneracy of the ground term. [c]Model: m - monomer, d - dimer (with $J > 0$); zfs - zero-field splitting, GFL - Griffith−Figgis−Lines model. Energies of four lowest Kramers doublets within the GFL model: for **1**: 0, 179, 363, 557; for **2**: 0, 78, 426, 509 cm$^{-1}$.

pyramidal geometries, while compounds **1** and **3** are closer to ideal SPY and TBY, respectively. As shown in the shape map of the minimum distortion interconversion path SPY/TBY (Figure S1), the experimental geometries of all these complexes significantly deviate from the Bailar path. It is attributable to the inequality in bond distances (especially in **1**, with Co−N bonds much shorter than Co−Cl ones), bending the moiety Co−N−CX, as well as to the constraints imposed by the chelate rings leading to Y- or T-type distortions. In complexes **2** and **3**, one equatorial bond angle decreases from that of the ideal trigonal bipyramid (120°), while two equivalent angles ă become larger than 120° [106.01(17)°, 123.76(14)°, and 128.89(14)° in **2** and 113.37(9)°, 122.94(7)°, and 122.94(7)° in **3**], indicating Y-type distortion.[49] For **1**, the angles Cl(1)−Co(1)−Cl(1), Cl(2)−Co(1)−N(1), and Cl(1)−Co(1)−N(1) are equal to 113.96(5)°, 104.66(10)°, and 141.8(4)°, respectively. The deviation from the Bailar path increases in the order $Cl^-$ < $NCS^-$ < $NCO^-$.

More detailed structural comparisons among $[Co(L)Cl_2]$ and $[Co(L)(NCS)_2]$ complexes, where L represents tridendate N-donor ligand, are given in Table S2 and Table S3, respectively. The data demonstrate that the thiocyanate complexes with the pentacoordinate cobalt(II) atom are bound to three nitrogen atoms of the *terpy*-like ligand, $[Co(terpy)_2](NCS)_2]\cdot 1.5H_2O$,[38] $[Co(terpy)_2(NCO)_2]$,[55] $[Co(mpzpy)(SCN)_2]$,[56] $[Co(4\text{-}Clterpy)(SCN)_2]$,[57] $[Co(mpytrz)(SCN)_2]$,[58] and $[Co(bpp)(NCS)_2]$,[59] (where *terpy* = 2,2′:6′2′′-terpyridine; *mpzpy* = 2,6-bis(3,5-dimethylpyrazolyl)-pyridine; 4-Cl-*terpy* = 4′-chloro-2,2′:6′2′′-terpyridine; *mpytrz* = 2,4-bis(3,5-dimethyl-1*H*-pyrazol-1-yl)-6-diethylamino-1,3,5-triazine, *bpp* = 2,6-bis(2-benzimidazolyl)pyridine) have a



DOI: 10.1021/acs.inorgchem.8b01906
Inorg. Chem. 2018, 57, 12740−12755

tendency to form intermediate structures between square pyramid and trigonal bipyramid with values in the range $\tau$ = 0.30−0.65. A similar trend is observed for the chloride complexes $[Co(L)Cl_2]$ incorporating peripheral modified *terpy*-like ligands: $[Co(pyazatr)Cl_2]$,[60] $[Co(imterpy)Cl_2]$,[61] $[Co(pypzpy)Cl_2]$,[62] $[Co(pz3py)Cl_2]$,[62] $[Co(trimephpy)Cl_2]$,[63] $[Co(dimephpy)Cl_2]$,[63] $[Co(clmephpy)Cl_2]$,[63] and $[Co(isprpy)Cl_2]$[63] where *pyazatr*-4,4′-(pyridine-2,6-diyl)bis(1′,1′-dimethyl-3-azatricyclo[7.1.1.02,7]undeca-2,4,6-triene; *imterpy*-6-iminoformyl-2,2′:6′,2′′-terpyridine-(2,6-diisopropylanil); *pypzpy* = 2,6-bis(1-(pyridin-2-yl)pyrazol-3-yl)pyridine; *pz3py* − 2,6-bis(pyrazol-3-yl)pyridine, *trimephpy* = *N*,*N*′-bis(2,4,6-trimethylphenyl)pyridine-2,6-dicarboximidoyl dichloride, *dimephpy* = *N*,*N*′-bis(2,6- dimethylphenyl)pyridine-2,6-dicarboximidoyl dichloride, *clmephpy* = *N*,*N*′-bis(4-chloro-2,6-dimethyl- phenyl)pyridine-2,6-dicarboximidoyl dichloride, *isprpy* = *N*,*N*′-bis(2,6-diisopropyl)pyridine-2,6-dicarboximidoyl dichloride. In contrast, the planar bis(imino)pyridine pincer ligands in $[Co(isprpy)(NCS)_2]$[65] and $[Co(pzam)(NCS)_2]$[66] as well as *terpy* and *terpy*-like ligands $[Co(terpy)Cl_2]$,[38,67] $[Co(4\text{-}Clterpy)Cl_2]$,[68] and $[Co(hppzpy)Cl_2]$[69] favor a square pyramidal over a trigonal bipyramidal coordination geometry (where *isprpy* = [2,6-bis{1-[(2,6-diisopropylphenyl)imino]-ethyl}pyridine; *pzam* = bis(ethyl-pyrazol-1*H*-yl)amine; 4-Cl-*terpy* = 4′-chloro-2,2′:6′,2″-terpyridine; *hppzpy* = 4-hept-1-ynyl-2,6-dipyrazol-1-ylpyridine). A slightly distorted TBY geometry is rather rare; it has been reported for $[Co(mepzea)(NCS)_2]$,[70] $[Co(bzmpzam)(NCS)_2]\cdot 0.75(CH_3)_2CO$,[71] and $[Co(mepzam)(NCS)_2]$;[72] (where *mepzea* = bis(2-(di-3,5-dimethyl-1-pyrazolyl)ethyl)amine; *bzmpzam* = *N*-benzyl-bis-(3,5-dimethyl-2-(pyrazol-1H-yl)ethyl)amine; *mepzam* = *N*,*N*-bis(3,5-dimethylpyrazol-1-ymethyl) amine) as well as for Co(II) complexes with pyrazolyl tripod ligands $[Co(bpdmpz)Cl]ClO_4$,[64] $[Co(bpdmpz)Cl]PF_6$,[64] $[Co(bdmpzp)Cl]ClO_4\cdot H_2O$,[64] $[Co(bdmpzp)Cl]ClO_4$,[64] $[Co(tdmpza)Cl]PF_6$;[64] *bpdmpz* = bis[(2-pyridylmethyl)-(di(3,5-dimethyl-1*H*-pyrazolyl)methyl)]amine; *bdmpzp* = bis[(di(3,5-dimethyl-1*H*-pyrazolyl)methyl))-(2-pyridylmethyl)]amine; *tdmpza* = tris-[di(3,5-dimethyl-1*H*-pyrazolyl)methyl)]amine.

***Ab Initio* Calculations.** *Ab initio* calculations were performed with the ORCA 4.0.0 computational package[73] using the experimental geometries determined by the X-ray diffraction for mononuclear entities. The relativistic effects were included in the calculations with zero order regular approximation (ZORA) together with the scalar relativistic contracted version of def2-TZVPP basis functions for the Co atom, def2-TZVP(-f) basis functions for the N, S, O atoms, and def2-SV(P) basis functions for other elements. The calculations of ZFS parameters were based on state average complete active space self-consistent field (SA-CASSCF) wave functions complemented by N-electron valence second order perturbation theory (NEVPT2).[74−78] The active space of the CASSCF calculations comprised of seven electrons in five metal-based d-orbitals. The state averaged approach was used, in which all 10 quartet and 40 doublet states were equally weighted. The calculations utilized the RI approximation with appropriate decontracted auxiliary basis set and the chain-of-spheres (RIJCOSX) approximation to exact exchange. Increased integration grids (Grid4 and GridX5) and tight SCF convergence criteria were used. The ZFS parameters were calculated through the quasi-degenerate perturbation theory in which an approximation to the Breit-Pauli form of the spin−orbit coupling operator (SOMF), and the effective Hamiltonian theory was utilized.[79−81] The principal results are contained in Table 2.

It is seen that the ground state in **1** is separated from the first excited one by a gap $\Delta_1$ = 717 $cm^{-1}$, which is in agreement with its quasi-degeneracy related to the $^4E$ term in the idealized $C_{4v}$ symmetry. The second excited state is well separated at $\Delta_2$ = 2219 $cm^{-1}$ so that four Kramers doublets dominate the magnetic properties of **1**. In **3** only the ground term $^4A_2$" in the idealized symmetry $D_{3h}$ contributes to the magnetic properties, and the spin-Hamiltonian formalism is fully applicable. The energy gap relates to the zero-field splitting parameter $\delta_1 \approx 2D$.

The calculated energy gap between the lowest crystal-field multiplets (abbr. $\delta_1$) has been plotted versus the Addison geometry parameter $\tau$, as displayed in Figure 2. This can be viewed as a type of the magnetostructural D-correlation where the parameter influencing the magnetic properties relates to the structural parameter.

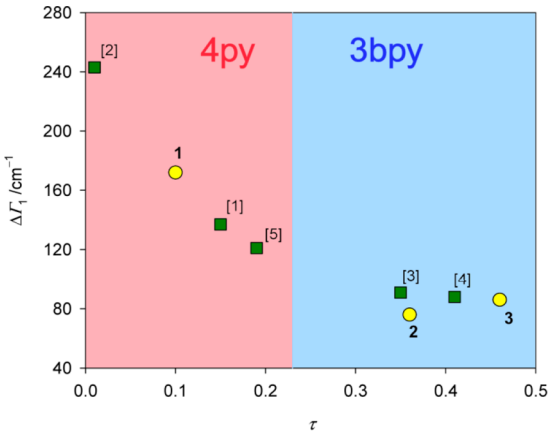


**Figure 2.** Correlation of the calculated (CASSCF/NEVPT2) energy of second lowest Kramers doublet (2*D* or $\delta_1$) and Addison $\tau$ parameter for complexes under study.

**DC Susceptibility.** The molar magnetic susceptibility has been converted to the effective magnetic moment whose temperature dependence is displayed in Figure 3 - left. The field dependence of the magnetization per formula unit $M_1 = M_{mol}/N_A\mu_B$ at the constant temperature is shown in Figure 3 - right.

At room temperature, the effective magnetic moment for **1** is $\mu_{eff} = g_{eff}[S(S+1)]^{1/2}$ = 5.12 $\mu_B$, which for the $S$ = 3/2 system yields $g_{eff}$ = 2.64. On cooling the effective magnetic moment passes through a broad maximum and finally it drops to 4.04 $\mu_B$ at $T$ = 1.8 K. Such a behavior is consistent with the involvement of the orbital angular momentum of the ground (octahedral) $^4T_1$ term. The geometry of the complex which is close to the tetragonal pyramid ($\tau$ = 0.10) implies that the ground term is the orbitally degenerate $^4E$ followed by the close-lying $^4A_1$. In such a case, the appropriate Hamiltonian refers to the generalized Griffith−Figgis−Lines (hereafter GFL) model working in the basis set of spin−orbit kets $|L = 1, M_L, S, M_S\rangle$, i.e.,

$$\hat{H}^{GF} = -(A\kappa\lambda)(\vec{L}_p\cdot\vec{S})\hbar^{-2} + \Delta_{ax}(\hat{L}_{p,z}^2 - \vec{L}_p^2/3)\hbar^{-2} + \Delta_{eq}(\hat{L}_{p,x}^2 - \hat{L}_{p,y}^2)\hbar^{-2} - \mu_B(A\kappa)(\vec{B}\cdot\vec{L}_p)\hbar^{-1} + \mu_B g_e(\vec{B}\cdot\vec{S})\hbar^{-1} \quad (2)$$



DOI: 10.1021/acs.inorgchem.8b01906
Inorg. Chem. 2018, 57, 12740−12755

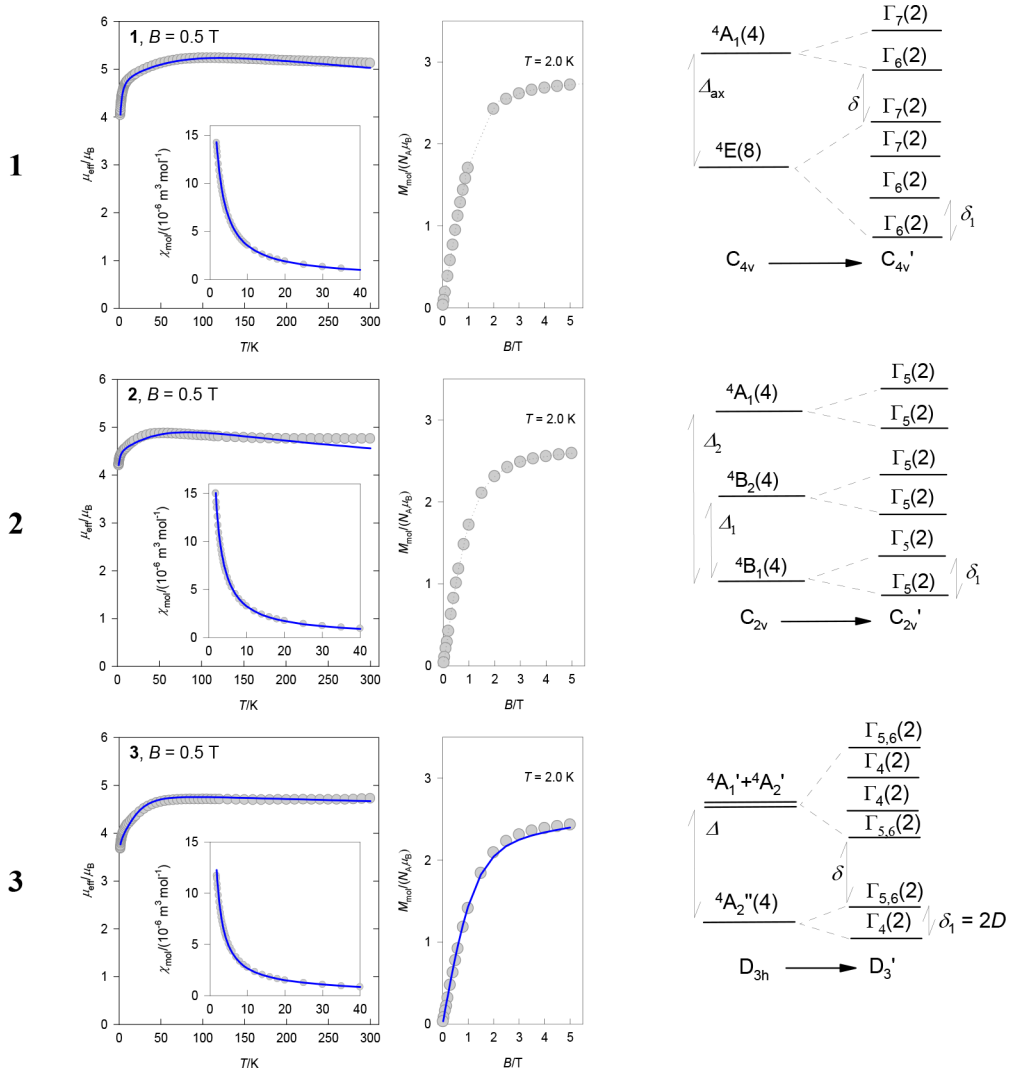


**Figure 3.** DC magnetic data for complexes **1** through **3**. Left - temperature dependence of the effective magnetic moment (inset shows the molar magnetic susceptibility); right - field dependence of the magnetization per formula unit. Solid lines - fitted. The lowest energy levels relevant to the magnetism are also drawn for idealized geometries.

It accounts for the spin−orbit coupling (the spin−orbit splitting parameter for free ion $\lambda = -\xi/2S = -155$ cm$^{-1}$), the axial and rhombic splitting parameters due to the crystal field of lower symmetry ($\Delta_{ax}$ and $\Delta_{rh}$), and the orbital and spin Zeeman terms. Here $\kappa$ is the orbital reduction factor, and $1 < A < 1.5$ is the Figgis CI parameter; owing to the $T$−$p$ isomorphism, the orbital angular momentum refers to $L_p = 1$. This Hamiltonian was treated in a fully numerical way. The susceptibility data were fitted with a reasonable set of magnetic parameters: $(A\kappa\lambda)/hc = -181$ cm$^{-1}$, $g_L = -(A\kappa) = -1.94$, $\Delta_{ax}/hc = -4000$ cm$^{-1}$, molecular-field correction $(zj/hc) = -0.073$ cm$^{-1}$, and the temperature-independent term $\chi_{TIM} = -5 \times 10^{-9}$ m$^3$ mol$^{-1}$ (the discrepancy factor $R(\chi) = 0.024$). Energies of four lowest Kramers doublets are 0, 179, 363, 557 cm$^{-1}$. A large negative value of $\Delta_{ax}$ means that the excited orbital singlet $^4A_1$ does not affect the magnetic data, which are determined exclusively by the orbital doublet $^4E$. The vanishing value of $\Delta_{rh}$ is consistent with the approximate $C_{4v}$ symmetry of a tetragonal pyramid. The first excitation energy has a relationship to *ab initio* NEVPT2 energy gap $\delta_1 = 172$ cm$^{-1}$ (see also Figure 3).

Complex **3** shows at room-temperature $\mu_{eff} = 4.72\ \mu_B$ ($g_{eff} = 2.44$) that stays constant down to $T \approx 50$ K; then it drops to $3.68\ \mu_B$ at $T = 1.8$ K. The magnetization per formula unit $M_1$ equals 2.43 at $T = 2.0$ K and $B = 5.0$ T. The data are consistent with the zero-field splitting (zfs) model described by the spin Hamiltonian

$$\hat{H}_a^S = D(\hat{S}_z^2 - \vec{S}^2/3)\hbar^{-2} + \mu_B B(\cos\vartheta_a g_z \hat{S}_z + \sin\vartheta_a g_x \hat{S}_x)\hbar^{-1} \quad (3)$$

where $D$ is the axial zero-field splitting parameter ($E$-parameter is omitted in order to avoid over-parametrization) and $a$ - direction of the magnetic field in the sense of polar coordinates; $\cos\vartheta_a$ is split into 15 grids for which the magnetization and susceptibility are averaged.[96] The optimization routine applied to the error functional consisting of relative errors of susceptibility and magnetization $F = E(\chi) + E(M)$ converged to the following set of magnetic parameters: $g_x = 2.65$, $D/hc = 30$ cm$^{-1}$, $(zj/hc) = -0.019$ cm$^{-1}$, and $\chi_{TIM} = -5 \times 10^{-9}$ m$^3$ mol$^{-1}$ ($R(\chi) = 0.029$ and $R(M) = 0.024$); $g_z = 2.0$ − fixed. The application of the zfs model is supported by the expected ground term $^4A_2$" for the geometry of the trigonal



DOI: 10.1021/acs.inorgchem.8b01906
Inorg. Chem. 2018, 57, 12740−12755

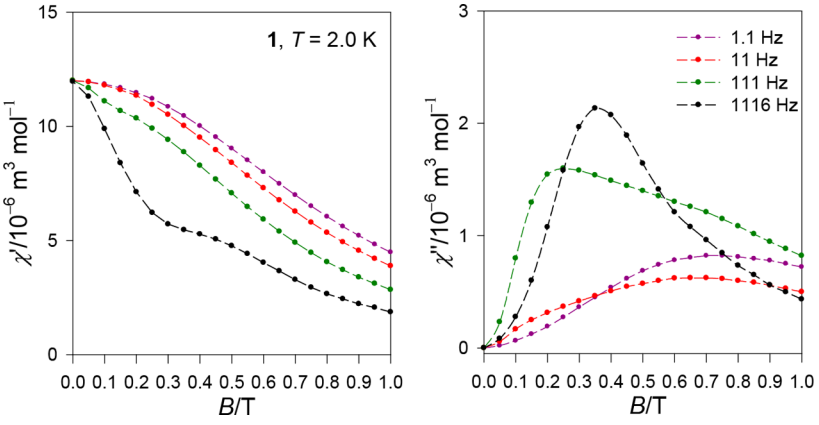


**Figure 4.** Field dependence of the AC susceptibility components for **1** at $T$ = 2.0 K for a set of frequencies of the AC field. Lines serve as a guide for the eyes.

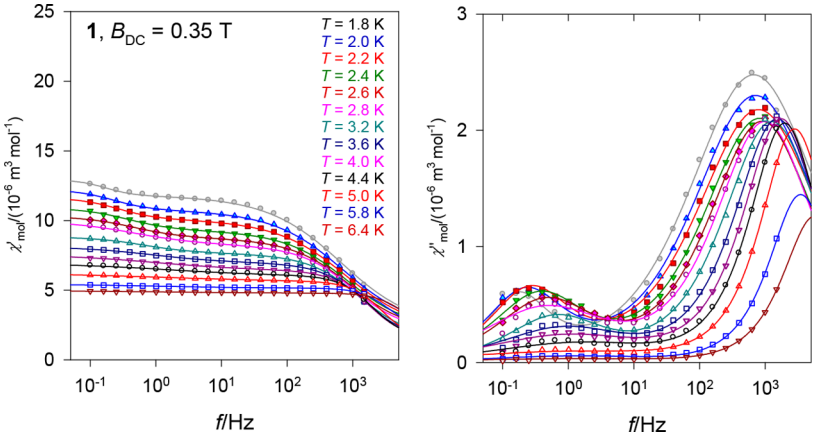


**Figure 5.** Frequency dependence of the AC susceptibility components for **1** at $B_{DC}$ = 0.35 T and fixed temperature. Lines - fitted.

bipyramid ($\tau$ = 0.46). Application of the GFL model with $\Delta_{ax} > 0$ providing a nondegenerate ground term fails in the sense that then the splitting parameter ($A\kappa\lambda$) converged to an unrealistic small value.

Magnetic properties of **2** lie somewhere in between **1** and **3** ($\tau$ = 0.36). A weak maximum at the $\mu_{eff}$ vs $T$ curve suggests that the generalized GFL and/or zfs model could be probed. The fitting procedure gave $(A\kappa\lambda)/hc = -130$ cm$^{-1}$, $g_L = -(A\kappa) = -1.97$, $\Delta_{ax}/hc = -8000$ cm$^{-1}$, $(zj/hc) = -0.029$ cm$^{-1}$, and the temperature-independent term $\chi_{TIM} = -11 \times 10^{-9}$ m$^3$ mol$^{-1}$ (the discrepancy factor $R(\chi)$ = 0.005). Again, a large negative value of $\Delta_{ax}$ causes a lift of the $^4A_1$ state outside thermal population. The zfs model is incapable of reproducing a broad maximum at the temperature dependence of the effective magnetic moment.

A comparison of data listed in Table 2 shows a great diversity of magnetic models and resulting magnetic parameter in the series of **1** through **3**, which is further enriched by data published previously for related complexes [1] − $[CoCl_2L^{C0}]_2$, [2] − $[CoCl_2L^{C7}]_2$, [3] − $[CoCl_2L^{C10}]_\infty$, [4] − $[CoCl_2L^{C12}]_\infty$, and [5] − $[CoCl_2L^{C14}]_2$ with the *para*-substituted pyridine ring by the alkyl chain C$^n$.[94] The situation is complicated by the fact that in all cases there are visible intermolecular interactions owing to the formation of supramolecular dimers and/or chains through the $\pi-\pi$ stacking of aromatic rings. Complexes with the geometry close to the tetragonal pyramid ($C_{4v}$, $\tau \approx 0$) possess the orbitally (quasi) degenerate ground term $^4E$ for which the Griffith−Figgis−Lewis model is appropriate. Rather problematic are the cases with $\tau$ = 0.3− 0.5 in which the orbital degeneracy is partially lifted: the ground term is orbitally nondegenerate; however, the first excited term is close lying, so that perturbation theory applied by means the spin Hamiltonian formalism could fail. This obstacle does not occur for the exact trigonal bipyramid ($D_{3h}$, $\tau \approx 1$), which is however not represented within the series of complexes under study.

**AC Susceptibility.** AC susceptibility data were acquired first at $T$ = 2.0 K for a set of representative frequencies of the alternating field ($f$ = 1.1, 11, 1111, and 1111 Hz) by ramping the magnetic field from zero to $B_{DC}$ = 0.5 T or even higher; the working amplitude $B_{AC}$ = 0.3 mT was used. Representative data for the complex **1** are displayed in Figure 4. There is no absorption signal (out-of-phase susceptibility component $\chi''$) at the zero field owing to a fast magnetic tunneling. With the increasing external field, this component raises, passes through a maximum, and then attenuates; such a behavior confirms that the complex **1** exhibits a field supported slow magnetic relaxation. The position of the maximum, however, visibly depends upon the frequency $f$ of the oscillating field.

Subsequent experiments were done for a fixed external magnetic field $B_{DC}$ = 0.35 T (at which there is a maximum of the high-frequency signal) by changing frequency between $f$ = 0.1 to 1500 Hz for a set of temperatures ranging between $T$ = 1.8 and 6.4 K (Figure 5). There are two relaxation modes: (i) the low-frequency (LF) mode occurs at $f \approx 0.5$ Hz, which implies the relaxation time $\tau(LF) = 1/(2\pi f'_{max}) = 0.3$ s; (ii) the



DOI: 10.1021/acs.inorgchem.8b01906
Inorg. Chem. 2018, 57, 12740−12755

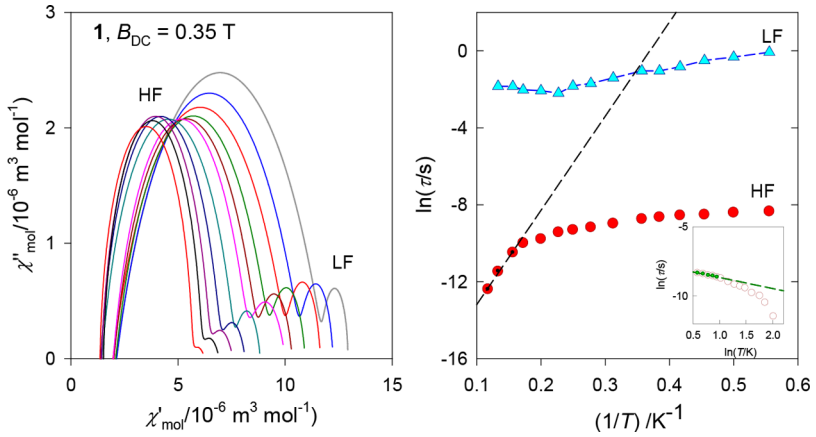


**Figure 6.** Argand diagram (left) and the Arrhenius-like plot (right) for **1**. Orbach-process parameters in the high-temperature limit, $\tau = \tau_0 \exp(U/k_BT)$: $U/k_B$ = 49 K, $\tau_0 = 1.4 \times 10^{-8}$ s. Raman process parameters in the low-temperature limit, $\tau^{-1} = CT^n$: $n$ = 0.8, $C$ = 2618 K$^{-n}$ s$^{-1}$ (inset).

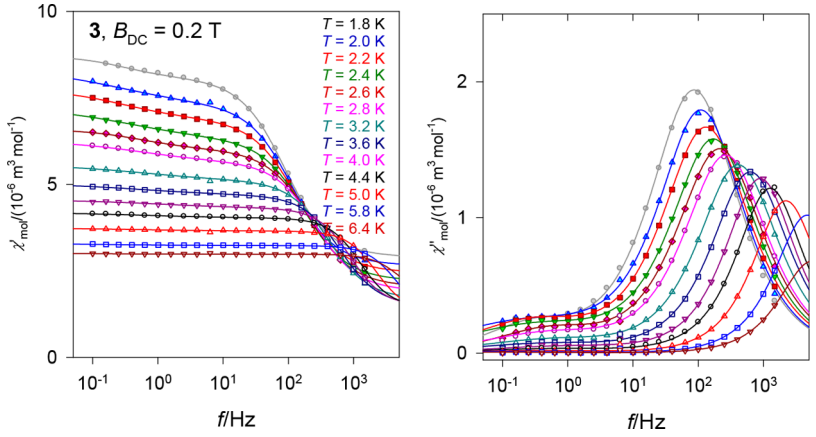


**Figure 7.** Frequency dependence of the AC susceptibility components for **3** at $B_{DC}$ = 0.2 T and fixed temperature. Lines - fitted.

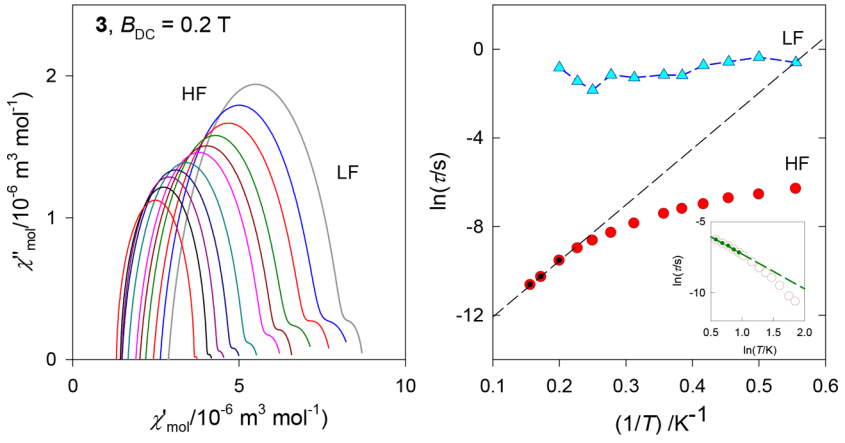


**Figure 8.** Argand diagram (left) and the Arrhenius-like plot (right) for **3**. Orbach-process parameters in the high-temperature limit $\tau = \tau_0 \exp(U/k_BT)$: $U/k_B$ = 25.3 K, $\tau_0 = 4.5 \times 10^{-7}$ s. Raman process parameters in the low-temperature limit, $\tau^{-1} = CT^n$: $n$ = 2.4, $C$ = 128 K$^{-n}$ s$^{-1}$ (inset).

high-frequency (HF) mode refers to the peak at $f \approx 1500$ Hz, so that $\tau$(HF) < $1 \times 10^{-4}$ s above $T > 1.8$ K. The heights of the peaks, $\chi_{LF}$ and $\chi_{HF}$, determine the mole fraction of the respective fraction: $x_{LF} = (\chi_{LF} - \chi_S)/(\chi_{HF} - \chi_S)$, where $\chi_S$ is the adiabatic susceptibility (the high-frequency limit). With increasing temperature, $x_{LF}$ decreases, while $x_{HF}$ increases according to $x_{HF} = 1 - x_{LF}$. On heating the position of the high-frequency peak is shifted to higher frequencies which is the usual behavior of SMMs and SIMs.

The AC susceptibility data were fitted by employing the two-set Debye model

$$\chi(\omega) = \chi_S + \frac{\chi_{LF} - \chi_S}{1 + (i\omega\tau_{LF})^{1-\alpha_{LF}}} + \frac{\chi_{HF} - \chi_{LF}}{1 + (i\omega\tau_{HF})^{1-\alpha_{HF}}} \quad (4)$$

that can be decomposed to the pure real and imaginary parts. Seven free parameters ($\chi_S$, isothermal susceptibilities $\chi_{LF}$, $\chi_{HF}$, distribution parameters $\alpha_{LF}$, $\alpha_{HF}$, relaxation times $\tau_{LF}$, and $\tau_{HF}$)



DOI: 10.1021/acs.inorgchem.8b01906
Inorg. Chem. 2018, 57, 12740−12755

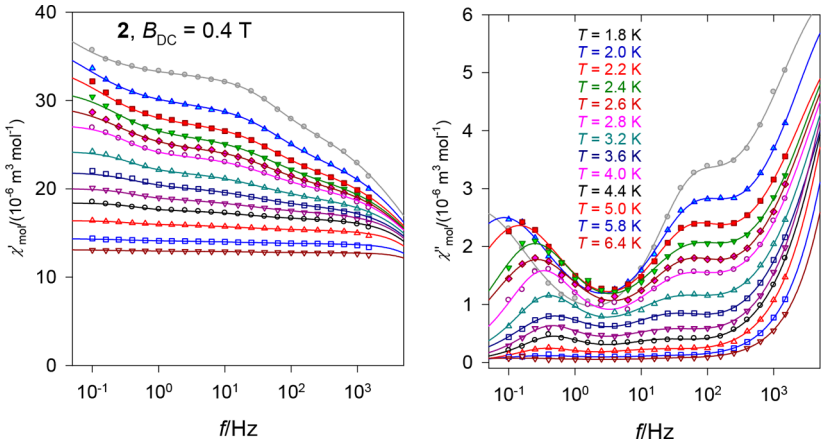


**Figure 9.** Frequency dependence of the AC susceptibility components for **2** at $B_{DC}$ = 0.4 T and fixed temperature. Lines - fitted.

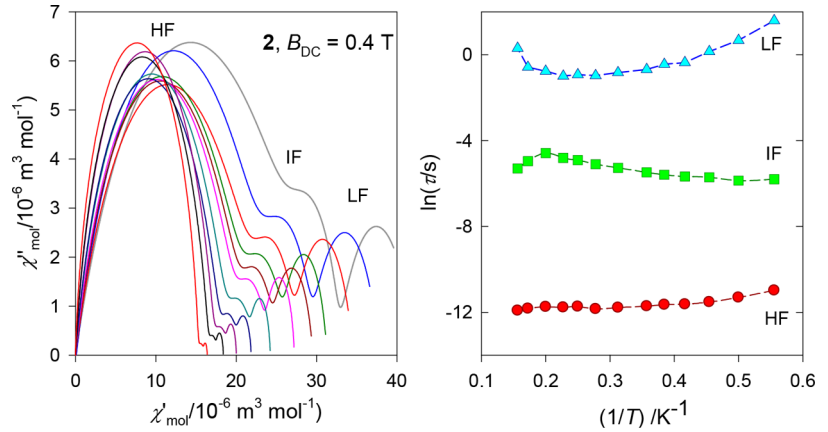


**Figure 10.** Argand diagram (left) and the Arrhenius-like plot (right) for **2**. Lines serve as a guide for the eyes.

**Table 3. Comparison of Key Characteristics of Related Complexes**[a]

| no. | geometry ($\tau$) | supra-molecular assembly | exchange ($J/hc$)/$cm^{-1}$ | (LF)-(HF) overlap | $B_{DC}$/T | $\tau_{LF}$@1.9K/ms | $\tau_{HF}$@1.9K/ms | $\chi_S$ |
|---|---|---|---|---|---|---|---|---|
| **1** | 4py, (0.10) | dimers | $J \approx 0$ | no | 0.35 | 930 | 0.22 | >0 |
| **2** | 3bpy, (0.36) | chains | $J \approx 0$ | yes, IF | 0.40 | 1951 | 2.86/0.0123 | [0] fixed |
| **3** | 3bpy, (0.46) | chains | $J \approx 0$ | yes | 0.20 | 690 | 1.43 | >0 |
| [1] | 4py, (0.15) | dimers | $J \approx 0$ | yes | 0.20 | 19.7 | 0.50 | >0 |
| [2] | 4py, (0.01) | dimers | 1.45 | no | 0.20 | 504 | 0.022 | [0] fixed |
| [3] | 3bpy, (0.35) | chains | 1.42 | no | 0.20 | 197 | 0.014 | [0] fixed |
| [4] | 3bpy, (0.41) | chains | $J \approx 0$ | yes | 0.20 | 32 | 2.12 | >0 |
| [5] | 4py, (0.19) | dimers | 1.06 | no | 0.20 | 404 | 0.0056 | [0] fixed |

[a]SPY = 4py = tetragonal (square) pyramid; TBY = 3bpy = trigonal bipyramid. Complexes studied previously: [1] – $[CoCl_2L^{C0}]_2$, [2] – $[CoCl_2L^{C7}]_2$, [3] – $[CoCl_2L^{C10}]_\infty$, [4] – $[CoCl_2L^{C12}]_\infty$, [5] – $[CoCl_2L^{C14}]_2$ with *para*-substituted pyridine ring by alkyl chain.[82] (LF) – slower, low-frequency relaxation mode, (HF) – faster, high-frequency relaxation mode.

can be fitted reliably by using 44 experimental data points. The quality of the fit was checked by the discrepancy factors $R(\chi')$ and $R(\chi'')$ along with standard deviations for each parameter (see Supporting Information). On the basis of quantitative assessment the relaxation time for the LF channel is as long as $\tau_{LF}$ = 0.72(6) s and that for the HF is as short as $\tau_{HF}$ = 0.22(1) ms at $T$ = 2.0 K, and $x_{LF}$ = 0.15.

The relaxation times enter the Arrhenius-like plot ln $\tau$ vs $T^{-1}$ that is displayed in Figure 6. This can be utilized in determining the relaxation parameters for the Orbach process in the high-temperature limit: the barrier to spin reversal $U/k_B$ = 49 K. This value needs be considered as an estimate since the maximum of the corresponding AC susceptibility component falls above the hardware limit (1500 Hz). The curved part of the Arrhenius-like plot can be recovered by considering the Raman process of the relaxation using linearized form of $\tau^{-1} = CT^n$.

The occurrence of two relaxation channels in small Co(II) based SIMs is now a frequent observation.[83−91] Owing to the presence of aromatic rings, these systems exhibit a rich system of intermolecular short contacts, such as hydrogen bonds, $\pi-\pi$ stacking, $\pi$−H interactions, etc. On cooling, they cause formation of oligonuclear entities (blocks, plaquettes, and finite chains), and such assemblies exhibit much slower spin relaxation than pure mononuclear entities.[92,93] This conclusion is supported by experiments with doping the complexes into


DOI: 10.1021/acs.inorgchem.8b01906
*Inorg. Chem.* 2018, 57, 12740−12755

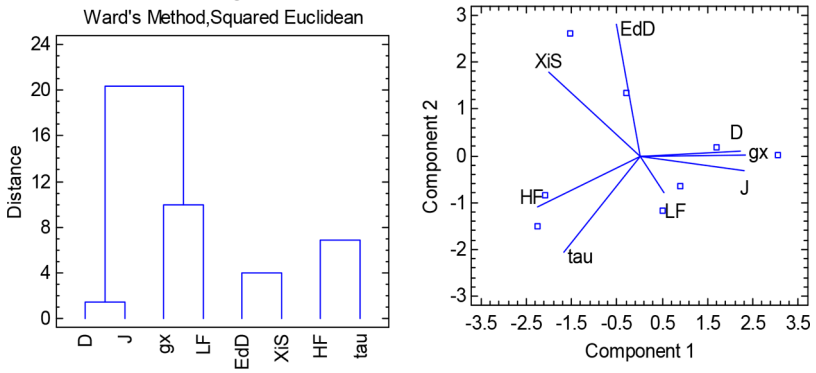


**Figure 11.** Distance dendrogram of the Cluster Analysis (left) and the biplot of the Principal Component Analysis (right) for complexes **1**, **2**, **3**, and [1] through [5].

the diamagnetic Zn matrix and also by the strong support of the LF relaxation channel by the external magnetic field.

The methodology of data taking and its analysis for the complex **3** is essentially similar to that described above. The complex **3** also shows the field-supported slow magnetic relaxation as evidenced from the field/temperature/frequency dependence of the AC magnetic susceptibility shown in Figures 7 and 8. The relaxation time for the LF channel is as long as $\tau_{LF}$ = 0.69(27) s and that for the HF is as short as $\tau_{HF}$ = 1.43(2) ms at $T$ = 2.0 K; the mole fraction $x_{LF}$ = 0.19.

The dynamic magnetic properties of the complex **2** are somewhat different from **1** and **3** in the sense that three relaxation channels are evident (Figures 9 and 10): in addition to the LF and HF relaxation channels also an intermediate-frequency (IF) channel is opened. This complex exhibits the longest LF mode relaxation time: $\tau_{LF}$ = 1.9(4) s at $T$ = 2.0 and $B_{DC}$ = 0.4 T.

The dynamic magnetic properties of three complexes under study can be compared to five analogous systems possessing pyridine ring *para*-substituted either by iodine or by a long alkyl chain (Table 3). The situation is very complicated by assembling the individual complexes to supramolecular dimers and/or chains. All these complexes exhibit two relaxation modes of different extents. The complexes with a geometry of square pyramid always form head-to-head dimers: **1**, [1], [2], and [5]. There is a ferromagnetic coupling in three cases [2], [3], and [5], which is well seen at the temperature evolution of the effective magnetic moment so that these systems have to be treated as dimers. In these cases, the HF mode is lifted above 1500 Hz, giving rise to the relaxation time of the order of $\mu$s. (Consequently, the adiabatic susceptibility needs be fixed to the zero.) In the remaining five systems, the exchange coupling is either very small or of the antiferromagnetic nature.

The available data, such as $\tau$, $J$, $g_x$, $D$, $E/D$ (abbr. EdD), $\tau_{LF}$ (abbr. LF), $\tau_{HF}$ (abbr. HF), and $\chi_S$ (abbr. XiS) has been subjected to statistical multivariate methods, namely, the Cluster Analysis (CA) and Principal Component Analysis (PCA); Figure 11. Closely related variables are grouped into three clusters. The purpose of the PCA is to obtain a small number of linear combinations of the eight variables which account for most of the variability in the data. In this case, three components have been extracted, since three components had eigenvalues greater than or equal to 1.0; together they account for 91% of the variability in the original data. This procedure allows unhide latent correlations among parameters. To this end, the Addison $\tau$ parameter correlates with the relaxation time $\tau_{HF}$. Three magnetic parameters are closely related: $J$, $g_x$, and $D$.

**EPR and Far-Infrared Magnetic Spectroscopy (FIRMS) Studies.** To further characterize the compounds under discussion, high-field EPR spectra were recorded as shown in Figure 12. The splitting between the Kramers doublets of the

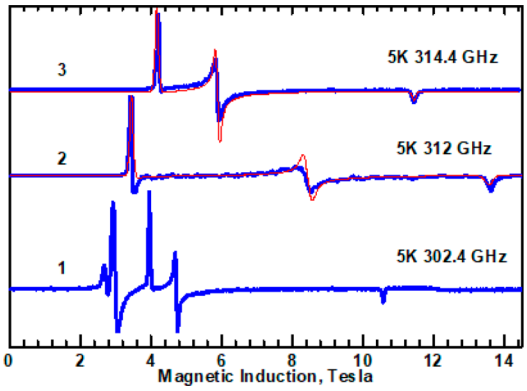


**Figure 12.** Blue traces: HF EPR spectra of the three compounds recorded at similar conditions. The red traces were simulated with $D$ = 40.92 cm$^{-1}$, $E$ = 3.18 cm$^{-1}$, $g_x$ = 2.175, $g_y$ = 2.43, $g_z$ = 2 for **3**, and $D$ = 38.4 cm$^{-1}$, $E$ = 9.8 cm$^{-1}$, $g_x$ = 2.18, $g_y$ = 2.46, $g_z$ = 2 for **2**.

3/2 spin state is very large as shown by the magnetic studies above and is much larger than the microwave quantum energy at the highest frequencies available to us, like 640 GHz. In a such situation, only the effective $g$ values are seen in the EPR spectra. In the axial case ($E$ = 0, $g_x$ = $g_y$), two features are seen in EPR. One of them appears close to the magnetic field corresponding to the intrinsic $g_z$ value, while another one is located close to the magnetic field corresponding to a doubled intrinsic $g_x$ value. Both features are due to transitions within the lower Kramers doublet, with $M_S$ = ±1/2. Three features are seen when $E \neq 0$ and their effective $g_x$, $g_y$, and $g_z$ values depend on the $E/D$ ratio, but simulations with (for example) $E$ = 10, $D$ = 50 cm$^{-1}$, and $E$ = 100, $D$ = 500 cm$^{-1}$ will be equal. All three complexes exhibited strongly nonaxial HF EPR spectra. The resonance position versus the microwave frequency dependencies over the range 200−630 GHz allowed determination of the $E/D$ ratio. For **3**, three effective $g$ values are observed, equal to 5.293, 3.825, and 1.964. Assuming the intrinsic $g_z$ = 2 (see above), the $E/D$ ratio of 0.078 is obtained (see Figure 12).



DOI: 10.1021/acs.inorgchem.8b01906
*Inorg. Chem.* 2018, 57, 12740−12755

Since only the $E/D$ ratio can be determined from EPR, far-infrared magnetic spectroscopy (FIRMS) studies were attempted to find the inter-Kramers energy separation at a zero magnetic field, which in the $S = 3/2$ state equals $\Delta E = 2(D^2 + 3E^2)^{1/2}$. In FIRMS, a sweep at terahertz frequencies is applied to a system, and absorption is measured as a function of frequency. Typically, very many features are observed, and to recognize the magnetic transitions under interest, many frequency-swept spectra are recorded at different magnetic fields, and transitions whose positions depend on the magnetic field are picked out. For **3**, the transition under question starts in zero magnetic field at 81.5 $cm^{-1}$ (Figure 13). Knowing the

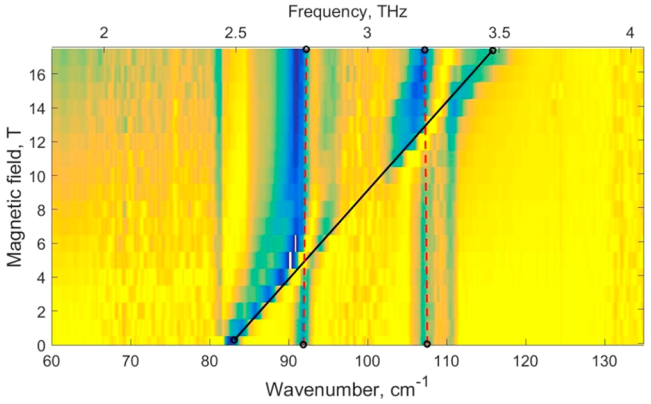


**Figure 13.** A color map of FIRMS resonances observed for **3** at 5 K showing a zero-field transition at 81.5 $cm^{-1}$ evolving into powder patterns with an applied magnetic field. The tendency toward the blue color means the absorbance increases, whereas the yellow color corresponds to the transparent regions.

inter-Kramers separation from FIRMS and the $E/D$ ratio from HFEPR, one can evaluate both $D$ and $E$. For **3** one obtains $D$ = 40.92 $cm^{-1}$, $E$ = 3.18 $cm^{-1}$, $g_x$ = 2.175, $g_y$ = 2.43, $g_z$ = 2. These parameters simulate EPR spectra at all frequencies, including FIRMS (Figure 14). However, the magnetic properties are not reproduced.

The HF EPR spectra of **2** are much more nonaxial than those of **3**. The effective $g$ values are 6.52, 2.66, and 1.64. The

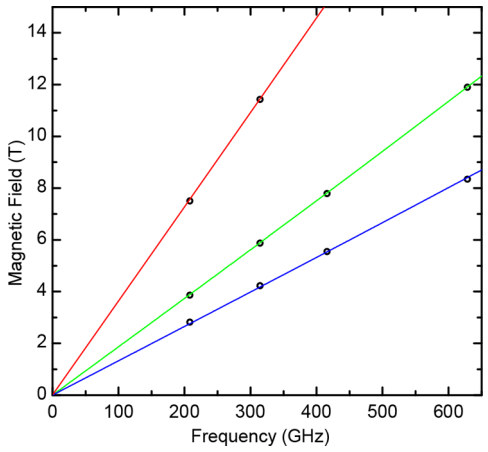


**Figure 14.** HF EPR resonances as a function of the microwave frequency for **3**. Circles: experimental points. The solid lines are calculated with $D$ = 40.92 $cm^{-1}$, $E$ = 3.18 $cm^{-1}$, $g_x$ = 2.175, $g_y$ = 2.43, $g_z$ = 2. The red, blue, and green lines correspond to the molecular orientations $Z$, $Y$, and $X$, respectively.

spin Hamiltonian approach may not be applicable in this case (see above). If we still try anyway, then assuming $g_z = 2$, we can estimate from the frequency dependencies shown in Figure 15

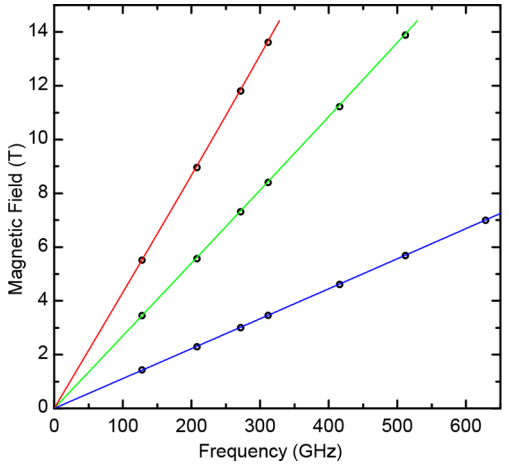


**Figure 15.** HF EPR resonances as a function of the microwave frequency for **2**. Circles: experimental points. The solid lines are calculated with $D$ = 38.4 $cm^{-1}$, $E$ = 9.8 $cm^{-1}$, $g_x$ = 2.18, $g_y$ = 2.46, $g_z$ = 2. The red, blue, and green lines correspond to the molecular orientations $Z$, $Y$, and $X$, respectively.

$g_x$ = 2.18, $g_y$ = 2.46, as well as the $E/D$ ratio of 0.256. This is thus the case of almost maximum rhombicity (for which $E/D$ = 1/3). In FIRMS, a zero-field transition is observed at 84 $cm^{-1}$ or 2520 GHz. This is in reasonable agreement with the splitting of 78 $cm^{-1}$ between the lowest Kramers doublets obtained from the magnetic data (see above). A calculation like the one presented above leads to $D$ = 38.4 $cm^{-1}$, $E$ = 9.8 $cm^{-1}$. Both HFEPR and FIRMS data are well simulated using these parameters, but the magnetic susceptibility data cannot be satisfactorily reproduced.

In the FIRMS spectrum of **1** (Figure 16), a transition is seen which at zero magnetic field occurs at ~158 $cm^{-1}$, at a much higher frequency than observed for **2** and **3**. The splitting between the two lowest Kramers doublets calculated from the magnetic data (see above) is 179 $cm^{-1}$, in reasonable agreement with the FIRMS result.

As shown in Figure 12, the HF EPR spectra of **1** are very different from those of the remaining two complexes. A large number of resonances are observed at some frequencies. There is a group of three resonances, seen in Figure 12 at 4, 4.8, and 10.5 T, whose effective $g$ values of 5.45, 4.55, and 2.035 are frequency-independent. Unlikely the other two complexes, **1** exhibits additional major resonances at a lower magnetic field of ca. 3 T in Figure 12. The distance between these two lowest field resonances is about 2500 Gauss and is frequency-independent (Figure 17), thus indicating a zero-field splitting. The effective $g$ value read out in the middle between these lowest-field resonances equals 7.66. That 2500 G splitting is presumably associated with the presence of quasi-dimers in the lattice, in which the Co−Co distance equals 6.16 A. An effective $g$ value as large as observed here can be generated from the intrinsic $g_x$, $g_y$ values on the order of 2.8 when the $E/D$ ratio is close to 1/3.

To account for the zero-field splitting, one could try the spin Hamiltonian for a dimer with large $D$ and $E$ on each $Co^{2+}$ ion and a small interaction between them, represented by terms containing $J$, $D_{12}$, and $E_{12}$, i.e.,


DOI: 10.1021/acs.inorgchem.8b01906
Inorg. Chem. 2018, 57, 12740−12755

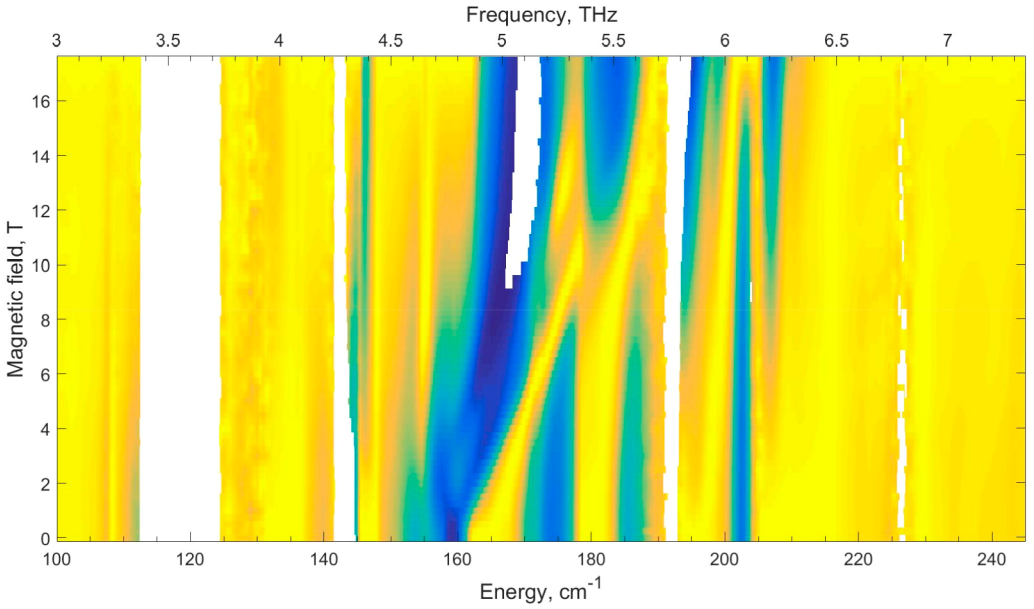


**Figure 16.** A color map of FIRMS resonances observed for **1** at 5 K showing a zero-field transition at 158 $cm^{-1}$ evolving into powder patterns with an applied magnetic field. The tendency toward the blue color means the absorbance increases, whereas the yellow color corresponds to the transparent regions.

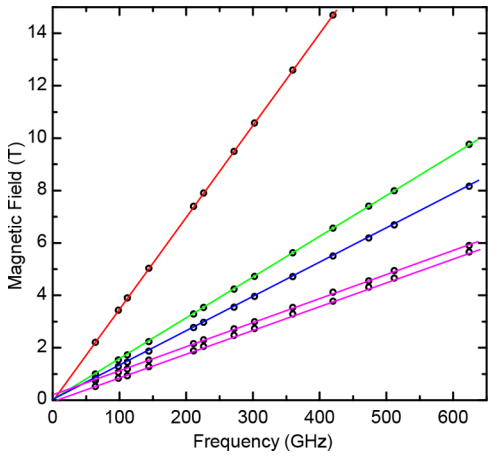


**Figure 17.** Resonance field versus frequency dependencies of the five major features in the spectra of **1** (see Figure 12). It is seen that the branches represented by the blue, green, and red lines pass through the 0,0 point of the plot. The frequency-independent effective *g* values of 5.45, 4.55, and 2.035, respectively, can be calculated from the slopes of the straight lines. The lines representing the two lowest-field features in the spectra (see Figure 12) do not pass through the origin of coordinates, and the 2500 Gauss distance between them is frequency-independent.

$$\hat{\boldsymbol{H}} = -J\hat{\boldsymbol{S}}_1\hat{\boldsymbol{S}}_2 + \mu_B\boldsymbol{B}\{\boldsymbol{g}_1\}\hat{\boldsymbol{S}}_1 + \mu_B\boldsymbol{B}\{\boldsymbol{g}_2\}\hat{\boldsymbol{S}}_2 + D_{Co}\left\{\hat{\boldsymbol{S}}_{z1}^2 - \frac{1}{3}S(S+1)\right\} + E_{Co}(\hat{\boldsymbol{S}}_{x1}^2 - \hat{\boldsymbol{S}}_{y1}^2) + D_{Co}\left\{\hat{\boldsymbol{S}}_{z2}^2 - \frac{1}{3}S(S+1)\right\} + E_{Co}(\hat{\boldsymbol{S}}_{x2}^2 - \hat{\boldsymbol{S}}_{y2}^2) + D_{12}\left\{\hat{\boldsymbol{S}}_{z1}\hat{\boldsymbol{S}}_{z2} - \frac{1}{3}\hat{\boldsymbol{S}}_1\hat{\boldsymbol{S}}_2\right\} + E_{12}(\hat{\boldsymbol{S}}_{x1}\hat{\boldsymbol{S}}_{x2} - \hat{\boldsymbol{S}}_{y1}\hat{\boldsymbol{S}}_{y2}) \quad (5)$$

It turns out that when taking intrinsic $g_y = 2.8$ on each Co, $E_{Co}/D_{Co} = 1/3$ and $J = -0.14$ $cm^{-1}$ reproduces both the slopes and splitting between the purple lines in Figure 17. However, other features are not reproduced. Nevertheless, it should be emphasized that this frequency-independent 2500 G splitting indeed indicates a metal−metal interaction. As shown by the magnetic and FIRMS studies, the ground state of a single $Co^{2+}$ ion is a well isolated Kramers doublet which cannot undergo any zero-field splitting. Also, it is not possible to explain these two low-field features by assuming that each of the low-field lines belongs to a different $Co^{2+}$ site. In such cases, both their plots in Figure 17 should pass through the 0,0 point and the splitting should be proportional to the microwave frequency. Figures S5−S7 show four lowest energy levels of the quasi-dimer and explain how a small isotropic exchange interaction results in zero-field splitting effects. It is observed that the intensity of the lowest-field transition is suppressed both at the lowers temperatures and by using higher microwave frequencies, which result in higher resonance fields. These trends require a negative (antiferromagnetic) J (see Figures S5−S7). This complicated system requires more investigations which we are planning.

## CONCLUSIONS

Three pentacoordinate complexes of the type $[Co(pypz)X_2]$, where *pypz* is a tridentate ligand 2,6-bis(pyrazol-1-yl)pyridine and X = $Cl^-$, $NCS^-$, and $NCO^-$, adopt a geometry in between square pyramid and trigonal bipyramid with the Addison tetragonality parameter $\tau$ = 0.10, 0.36, and 0.46. The DC magnetic data show a sizable magnetic anisotropy, which was confirmed by high-field HF EPR measurement together with FIRM method, to determine the exact large *D* value for **2** (38.4 $cm^{-1}$) and **3** (40.92 $cm^{-1}$). The AC susceptibility data confirm that these complexes exhibit a slow magnetic relaxation under a small applied DC field with two relaxation modes. The low-frequency mode at $T$ = 2.0 K is as slow as $\tau_{LF}$ = 0.72(6) s, 1.9(4) s, and $\tau_{LF}$ = 0.69(27) s, respectively ($B_{DC}$ = 0.35, 0.40, and 0.20 T). Another aspect is represented by the fact that the negative values of *D* associated with the easy-axis of magnetization is also no longer an ultimate demand for



DOI: 10.1021/acs.inorgchem.8b01906
Inorg. Chem. 2018, 57, 12740−12755

SIMs behavior; there is much evidence for SMR in the case of $D > 0$, however, followed by some rhombic component E.[94,95] The result obtained for complexes **1**, **2**, and **3** fully confirms this hypothesis.

## ■ ASSOCIATED CONTENT

### Supporting Information

The Supporting Information is available free of charge on the ACS Publications website at DOI: 10.1021/acs.inorgchem.8b01906.

X-ray structural data, AC susceptibility data (PDF)

### Accession Codes

CCDC 1831188−1831190 contain the supplementary crystallographic data for this paper. These data can be obtained free of charge via www.ccdc.cam.ac.uk/data_request/cif, or by emailing data_request@ccdc.cam.ac.uk, or by contacting The Cambridge Crystallographic Data Centre, 12 Union Road, Cambridge CB2 1EZ, UK; fax: +44 1223 336033.

## ■ AUTHOR INFORMATION


### Corresponding Authors

*(A.S.) E-mail: anna.switlicka@us.edu.pl.
*(A.B.) E-mail: alina.bienko@chem.uni.wroc.pl.

### ORCID

Anna Świtlicka: 0000-0001-8192-5619
Mateusz Penkala: 0000-0001-8949-0322
Roman Boča: 0000-0003-0222-9434
Andrew Ozarowski: 0000-0001-6225-9796


### Notes

The authors declare no competing financial interest.

## ■ ACKNOWLEDGMENTS

This work was supported by the Polish National Science Centre (Grant No. 2015/17/D/ST5/01344; A.Ś.). Slovak grant agencies (APVV-14-0078, APVV 16-0039, VEGA 1/0919/17, and VEGA 1/0534/16; R.B.) are acknowledged for the financial support. The magnetic measurements was supported by Wroclaw Centre of Biotechnology, program The Leading National Research Centre (KNOW) for years 2014−2018. (A.B.) The National High Magnetic Field Laboratory is supported by National Science Foundation Cooperative Agreement No. DMR-1644779 and the State of Florida.

## ■ REFERENCES


(1) Affronte, M.; Troiani, F.; Ghirri, A.; Candini, A.; Evangelisti, M.; Corradini, V.; Carretta, S.; Santini, P.; Amoretti, G.; Tuna, F.; Timco, G.; Winpenny, R E. P. Single molecule magnets for quantum computation. *J. Phys. D: Appl. Phys.* **2007**, *40*, 2999−3004.

(2) Ardavan, A.; Rival, O.; Morton, J. J. L.; Blundell, S. J.; Tyryshkin, A. M.; Timco, G. A.; Winpenny, R. E. P. Will Spin-Relaxation Times in Molecular Magnets Permit Quantum Information Processing? *Phys. Rev. Lett.* **2007**, *98*, 057201.

(3) Bogani, L.; Wernsdorfer, W. Molecular Spintronics Using Single-Molecule Magnets. *Nat. Mater.* **2008**, *7*, 179−186.

(4) Sanvito, S. Molecule-based magnets themed issue. *Chem. Soc. Rev.* **2011**, *40*, 3336−3355.

(5) Lumetti, S.; Candini, A.; Godfrin, C.; Balestro, F.; Wernsdorfer, W.; Klyatskaya, S.; Ruben, M.; Affronte, M. Single-molecule devices with graphene electrodes. *Dalton Trans* **2016**, *45*, 16570−16574.

(6) Rocha, A. R.; García-Suárez, V. M.; Bailey, S. W.; Lambert, C. J.; Ferrer, J.; Sanvito, S. Towards molecular spintronics. *Nat. Mater.* **2005**, *4*, 335−339.

(7) Affronte, M. Molecular nanomagnets for information technologies. *J. Mater. Chem.* **2009**, *19*, 1731−1737.

(8) Sessoli, R.; Boulon, M.-E.; Caneschi, A.; Mannini, M.; Poggini, L.; Wilhelm, F.; Rogalev, A. Strong magneto-chiral dichroism in a paramagnetic molecular helix observed by hard X-rays. *Nat. Phys.* **2015**, *11*, 69−74.

(9) Ghirri, A.; Candini, A.; Affronte, M. Molecular Spins in the Context of Quantum Technologies. *Magnetochemistry* **2017**, *3* (1), 12.

(10) Cornia, A.; Seneor, P. Spintronics: The molecular way. *Nat. Mater.* **2017**, *16*, 505−506.

(11) Prezioso, M.; Riminucci, A.; Graziosi, P.; Bergenti, I.; Rakshit, R.; Cecchini, R.; Vianelli, A.; Borgatti, F.; Haag, N.; Willis, M.; Drew, A. J.; Gillin, W. P.; Dediu, V. A. Single-Device Universal Logic Gate Based on a Magnetically Enhanced Memristor. *Adv. Mater.* **2013**, *25*, 534−538.

(12) Sessoli, R.; Gatteschi, D.; Caneschi, A.; Novak, M. A. Magnetic bistability in a metal-ion cluster. *Nature* **1993**, *365*, 141−143.

(13) Sessoli, R.; Powell, A. K. Strategies towards single molecule magnets based on lanthanide ions. *Coord. Chem. Rev.* **2009**, *253*, 2328−2341.

(14) Murrie, M. Cobalt(II) single-molecule magnets. *Chem. Soc. Rev.* **2010**, *39*, 1986−1995.

(15) Jeon, I. R.; Clérac, R. Controlled association of single-molecule magnets (SMMs) into coordination networks: towards a new generation of magnetic materials. *Dalton Trans* **2012**, *41*, 9569−9586.

(16) Woodruff, D. N.; Winpenny, R. E. P.; Layfield, R. A. Lanthanide Single-Molecule Magnets. *Chem. Rev.* **2013**, *113*, 5110−5148.

(17) Liu, K.; Shi, W.; Cheng, P. Toward heterometallic single-molecule magnets: Synthetic strategy, structures and properties of 3d−4f discrete complexes. *Coord. Chem. Rev.* **2015**, *289−290*, 74−122.

(18) McAdams, S. G.; Ariciu, A. M.; Kostopoulos, A. K.; Walsh, J. P. S.; Tuna, F. Molecular single-ion magnets based on lanthanides and actinides: Design considerations and new advances in the context of quantum technologies. *Coord. Chem. Rev.* **2017**, *346*, 216−239.

(19) Ishikawa, N.; Sugita, M.; Ishikawa, T.; Koshihara, S.; Kaizu, Y. Lanthanide Double-Decker Complexes Functioning as Magnets at the Single-Molecular Level. *J. Am. Chem. Soc.* **2003**, *125*, 8694−8695.

(20) Gomez-Coca, S.; Cremades, E.; Aliaga-Alcalde, N.; Ruiz, E. Mononuclear Single-Molecule Magnets: Tailoring the Magnetic Anisotropy of First-Row Transition-Metal Complexes. *J. Am. Chem. Soc.* **2013**, *135*, 7010−7018.

(21) Craig, G. A.; Murrie, M. 3d single-ion magnets. *Chem. Soc. Rev.* **2015**, *44*, 2135−2147.

(22) Frost, J. M.; Harriman, K. L. M.; Murugesu, M. The rise of 3-d single-ion magnets in molecular magnetism: towards materials from molecules? *Chem. Sci.* **2016**, *7*, 2470−2491.

(23) Harriman, K. L. M.; Murugesu, M. An Organolanthanide Building Block Approach to Single-Molecule Magnets. *Acc. Chem. Res.* **2016**, *49*, 1158−1167.

(24) Ferrando-Soria, J.; Vallejo, J.; Castellano, M.; Martínez-Lillo, J.; Pardo, E.; Cano, J.; Castro, I.; Lloret, F.; Ruiz-García, R.; Julve, M. Molecular magnetism, quo vadis? A historical perspective from a coordination chemist viewpoint. *Coord. Chem. Rev.* **2017**, *339*, 17−103.

(25) Boeckmann, J.; Näther, C. Solid-state transformation of $[Co(NCS)_2(pyridine)_4]$ into $[Co(NCS)_2(pyridine)_2]_n$: from Curie−Weiss paramagnetism to single chain magnetic behavior. *Dalton Trans* **2010**, *39*, 11019−11026.

(26) Sun, H. L.; Wang, Z. M.; Gao, S. Strategies towards single-chain magnets. *Coord. Chem. Rev.* **2010**, *254*, 1081−1100.

(27) Liu, T.; Zheng, H.; Kang, S.; Shiota, Y.; Hayami, S.; Mito, M.; Sato, O.; Yoshizawa, K.; Kanegawa, S.; Duan, C. A light-induced spin crossover actuated single-chain magnet. *Nat. Commun.* **2013**, *4*, 2826.




DOI: 10.1021/acs.inorgchem.8b01906
*Inorg. Chem.* 2018, 57, 12740−12755

(28) Wöhlert, S.; Fic, T.; Tomkowicz, Z.; Ebbinghaus, S. G.; Rams, M.; Haase, W.; Näther, C. Structural and Magnetic Studies of a New Co(II) Thiocyanato Coordination Polymer Showing Slow Magnetic Relaxations and a Metamagnetic Transition. *Inorg. Chem.* **2013**, *52*, 12947−12957.
(29) Werner, J.; Rams, M.; Tomkowicz, Z.; Näther, C. A Co(II) thiocyanato coordination polymer with 4-(3-phenylpropyl)pyridine: the influence of the co-ligand on the magnetic properties. *Dalton Trans* **2014**, *43*, 17333−17342.
(30) Dhers, S.; Feltham, H. L.C.; Brooker, S. A toolbox of building blocks, linkers and crystallisation methods used to generate single-chain magnets. *Coord. Chem. Rev.* **2015**, *296*, 24−44.
(31) Ion, A. E.; Nica, S.; Madalan, A. M.; Shova, S.; Vallejo, J.; Julve, M.; Lloret, F.; Andruh, M. Two-Dimensional Coordination Polymers Constructed Using, Simultaneously, Linear and Angular Spacers and Cobalt(II) Nodes. New Examples of Networks of Single-Ion Magnets. *Inorg. Chem.* **2015**, *54*, 16−18.
(32) Ma, R.; Chen, Z.; Cao, F.; Wang, S.; Huang, X.; Li, Y.; Lu, J.; Li, D.; Dou. Two 2-D multifunctional cobalt(II) compounds: field-induced single-ion magnetism and catalytic oxidation of benzylic C−H bonds. *Dalton Trans* **2017**, *46*, 2137−2145.
(33) Palion-Gazda, J.; Klemens, T.; Machura, B.; Vallejo, J.; Lloret, F.; Julve, M. Single ion magnet behaviour in a two-dimensional network of dicyanamide-bridged cobalt(II) ions. *Dalton Trans* **2015**, *44*, 2989−2992.
(34) Świtlicka-Olszewska, A.; Palion-Gazda, J.; Klemens, T.; Machura, B.; Vallejo, J.; Cano, J.; Lloret, F.; Julve, M. Single-ion magnet behaviour in mononuclear and two-dimensional dicyanamide-containing cobalt(II) complexes. *Dalton Trans* **2016**, *45*, 10181−10193.
(35) Zadrozny, J. M.; Liu, J.; Piro, N. A.; Chang, C. J.; Hill, S.; Long, J. R. Slow magnetic relaxation in a pseudotetrahedral cobalt(II) complex with easy-plane anisotropy. *Chem. Commun.* **2012**, *48*, 3927−3929.
(36) Yang, F.; Zhou, Q.; Zhang, Y.; Zeng, G.; Li, G.; Shi, Z.; Wang, B.; Feng, S. Inspiration from old molecules: field-induced slow magnetic relaxation in three air-stable tetrahedral cobalt(II) compounds. *Chem. Commun.* **2013**, *49*, 5289−5291.
(37) Cao, D. K.; Feng, J. Q.; Ren, M.; Gu, Y. W.; Song, Y.; Ward, M. D. A mononuclear cobalt(II)−dithienylethene complex showing slow magnetic relaxation and photochromic behavior. *Chem. Commun.* **2013**, *49*, 8863−8865.
(38) Habib, F.; Luca, O. R.; Vieru, V.; Shiddiq, M.; Korobkov, I.; Gorelsky, S. I.; Takase, M. K.; Chibotaru, L. F.; Hill, S.; Crabtree, R. H.; Murugesu, M. Influence of the Ligand Field on Slow Magnetization Relaxation versus Spin Crossover in Mononuclear Cobalt Complexes. *Angew. Chem., Int. Ed.* **2013**, *52*, 11290−11293.
(39) Groom, C. R.; Bruno, I. J.; Lightfoot, M. P.; Ward, S. C. The Cambridge Structural Database. *Acta Crystallogr., Sect. B: Struct. Sci., Cryst. Eng. Mater.* **2016**, *72*, 171−179.
(40) Chakrabarty, S.; Poddar, R. K.; Poulsen, R. D.; Thompson, A. L.; Howard, J. A. K. The copper(II) complexes di-$\mu$-bromo-bis{[2,6-bis(pyrazol-1-yl)pyridine]perchloratocopper(II)} and [2,6-bis-(pyrazol-1-yl)pyridine]dibromocopper(II). *Acta Crystallogr., Sect. C: Cryst. Struct. Commun.* **2004**, *60*, m628−m630.
(41) Nian Yang, Z.; Sun, T. T. Dichlorido(2,6-dipyrazol-1-ylpyridine)zinc(II). *Acta Crystallogr., Sect. E: Struct. Rep. Online* **2008**, *64*, m1374.
(42) Gong, D.; Jia, X.; Wang, B.; Zhang, X.; Jiang, L. Synthesis, characterization, and butadiene polymerization of iron(III), iron(II) and cobalt(II) chlorides bearing 2,6-bis(2-benzimidazolyl)pyridyl or 2,6-bis(pyrazol)pyridine ligand. *J. Organomet. Chem.* **2012**, *702*, 10−18.
(43) Switlicka, A.; Czerwinska, K.; Machura, B.; Penkala, M.; Bienko, A.; Bienko, D.; Zierkiewicz, W. Thiocyanate copper complexes with pyrazole-derived ligands − synthesis, crystal structures, DFT calculations and magnetic properties. *CrystEngComm* **2016**, *18*, 9042−9055.
(44) Baum, G.; Blake, A. J.; Fenske, D.; Hubberstey, P.; Julio, C.; Withersby, M. A. (Acetonitrile)[2,6-bis(pyrazol-1-yl)pyridine]-(isonicotinamide)copper(II)-tetrafluoroborate-acetonitrile (1/2/2). *Acta Crystallogr., Sect. C: Cryst. Struct. Commun.* **2002**, *58*, m542−m544.
(45) *CrysAlis RED*, Version 1.171.29.2; Oxford Diffraction Ltd.; Sheldrick, G. M. Phase annealing in SHELX-90: direct methods for larger structures. *Acta Crystallogr.* 1990, *A46*, 467−473.
(46) *CrysAlis RED*, Version 1.171.35.11; Oxford Diffraction Ltd, 2011.
(47) Sheldrick, G. M. A short history of SHELX. *Acta Crystallogr., Sect. A: Found. Crystallogr.* **2008**, *64*, 112−122.
(48) Addison, A. W.; Rao, T. N.; Reedijk, J.; van Rijn, J.; Verschoor, G. C. Synthesis, structure, and spectroscopic properties of copper(II) compounds containing nitrogen−sulphur donor ligands; the crystal and molecular structure of aqua[1,7-bis(N-methylbenzimidazol-2′-yl)-2,6-dithiaheptane]copper(II) perchlorate. *J. Chem. Soc., Dalton Trans.* **1984**, 1349−1356.
(49) Macrae, C. F.; Bruno, I. J.; Chisholm, J. A.; Edgington, P. R.; McCabe, P.; Pidcock, E.; Rodriguez-Monge, L.; Taylor, R.; van de Streek, J.; Wood, P. A. Mercury CSD 2.0 − new features for the visualization and investigation of crystal structures. *J. Appl. Crystallogr.* **2008**, *41*, 466−470.
(50) Llunell, M.; Casanova, D.; Cirera, J.; Alemany, P.; Alvarez, S. *SHAPE* version 2.0; Universitat de Barcelona, 2010.
(51) Cirera, J.; Alemany, P.; Alvarez, S. Mapping the Stereochemistry and Symmetry of Tetracoordinate Transition- Metal Complexes. *Chem. - Eur. J.* **2004**, *10*, 190−207.
(52) Casanova, D.; Cirera, J.; Llunell, M.; Alemany, P.; Avnir, D.; Alvarez, S. Minimal Distortion Pathways in Polyhedral Rearrangements. *J. Am. Chem. Soc.* **2004**, *126*, 1755−1763.
(53) Cirera, J.; Ruiz, E.; Alvarez, S. Stereochemistry and Spin State in Four-Coordinate Transition Metal Compounds. *Inorg. Chem.* **2008**, *47*, 2871−2889.
(54) Alvarez, S.; Llunell, M. Continuous symmetry measures of penta-coordinate molecules: Berry and non-Berry distortions of the trigonal bipyramid. *J. Chem. Soc., Dalton Trans.* **2000**, 3288−3303.
(55) Kepert, D. L.; Kucharski, E. S.; White, A. H. Crystal Structure of Bis(isocyanato)(2,2′:6′,2″-terpyridyl)cobalt(II): Stereochemistry of [M(tridentate ligand)(unidentate ligand)$_2$] complexes. *J. Chem. Soc., Dalton Trans.* **1980**, 1932−1938.
(56) Arici, C.; Ulku, D.; Kurtaran, R.; Emregul, K. C.; Atakol, O. Synthesis, crystal structure and electrochemical behaviour of [2,6-bis(3,5-dimethylpyrazolyl)pyridine] (dithiocyanato)cobalt(II). *Z. Kristallogr. - Cryst. Mater.* **2003**, *218*, 497−500.
(57) Zhang, G.; Tan, J.; Zhang, Y. Z.; Ta, C.; Sanchez, S.; Cheng, S. Y.; Golen, J. A.; Rheingold, A. L. Syntheses, structures and cytotoxicity of cobalt(II) complexes with 4'-chloro-2,2':6',2''-terpyridine. *Inorg. Chim. Acta* **2015**, *435*, 147−152.
(58) Wang, X.; Xing, Y. H.; Bai, F. Y.; Wang, X. Y.; Guan, Q. L.; Hou, Y. N.; Zhang, R.; Shi, Z. Synthesis, structure, and surface photovoltage properties of a series of novel $d^7$−$d^{10}$ metal complexes with pincer N-heterocycle ligands. *RSC Adv.* **2013**, *3*, 16021−16033.
(59) Mondal, A. K.; Goswami, T.; Misra, A.; Konar, S. Probing the Effects of Ligand Field and Coordination Geometry on Magnetic Anisotropy of Pentacoordinate Cobalt(II) Single-Ion Magnets. *Inorg. Chem.* **2017**, *56*, 6870−6878.
(60) Yeung, C. T.; Sham, K. C.; Lee, W. S.; Wong, W. T.; Wong, W. Y.; Kwong, H. L. Cobalt and iron complexes of chiral $C_1$- and $C_2$-terpyridines: Synthesis, characterization and use in catalytic asymmetric cyclopropanation of styrenes. *Inorg. Chim. Acta* **2009**, *362*, 3267−3273.
(61) Champouret, Y. D. M.; Marechal, J. D.; Chaggar, R. K.; Fawcett, J.; Singh, K.; Maseras, F.; Solan, G. A. Factors affecting imine coordination in (iminoterpyridine)$MX_2$ (M = Fe, Co, Ni, Zn): synthesis, structures, DFT calculations and ethylene oligomerisation studies. *New J. Chem.* **2007**, *31*, 75−85.
(62) Dong, G.; Matthews, J. P.; Craig, D. C.; Baker, A. T. The syntheses, spectra and structures of five-coordinate cobalt(II)


DOI: 10.1021/acs.inorgchem.8b01906
*Inorg. Chem.* 2018, 57, 12740−12755

complexes of pyrazolyl-containing ligands. *Inorg. Chim. Acta* **1999**, *284*, 266−272.
(63) Nemec, I.; Liu, H.; Herchel, R.; Zhang, X.; Trávníček, Z. Magnetic anisotropy in pentacoordinate 2,6-bis(arylazanylidene-1-chloromethyl)pyridine cobalt(II) complexes with chlorido co-ligands. *Synth. Met.* **2016**, *215*, 158−163.
(64) Massoud, S. S.; Fischer, R. C.; Mautner, F. A.; Parfait, M. M.; Herchel, R.; Trávníček, Z. Pentacoordinate cobalt(II) complexes with neutral tripodal N-donor ligands: Zero-field splitting for a distorted trigonal bipyramidal geometry. *Inorg. Chim. Acta* **2018**, *471*, 630−639.
(65) Jurca, T.; Farghal, A.; Lin, P. H.; Korobkov, I.; Murugesu, M.; Richeson, D. S. Single-Molecule Magnet Behavior with a Single Metal Center Enhanced through Peripheral Ligand Modifications. *J. Am. Chem. Soc.* **2011**, *133*, 15814−15817.
(66) Massoud, S. S.; Dubin, M.; Guilbeau, A. E.; Spell, M.; Vicente, R.; Wilfling, P.; Fischer, R. C.; Mautner, F. A. Azido- and thiocyanato-cobalt(II) complexes based pyrazole ligands. *Polyhedron* **2014**, *78*, 135−140.
(67) Goldschmied, E.; Stephenson, N. C. The Crystal Structure of Dichloro-2,2″,2″-terpyridylcobalt(II). *Acta Crystallogr., Sect. B: Struct. Crystallogr. Cryst. Chem.* **1970**, *26*, 1867−1875.
(68) Zhang, G.; Tan, J.; Zhuo Zhang, Y.; Ta, C.; Sanchez, S.; Cheng, S. Y.; Golen, J. A.; Rheingold, A. L. Syntheses, structures and cytotoxicity of cobalt(II) complexes with 4′-chloro-2,2′:6′,2″-terpyridine. *Inorg. Chim. Acta* **2015**, *435*, 147−152.
(69) Rajnák, C.; Titiš, J.; Fuhr, O.; Ruben, M.; Boča, R. Single-Molecule Magnetism in a Pentacoordinate Cobalt(II) Complex Supported by an Antenna Ligand. *Inorg. Chem.* **2014**, *53*, 8200−8202.
(70) Massoud, S. S.; Le Quan, L.; Gatterer, K.; Albering, J. H.; Fischer, R. C.; Mautner, F. A. Structural characterization of five-coordinate copper(II), nickel(II), and cobalt(II) thiocyanato complexes derived from bis(2-(3,5-dimethyl-1-pyrazolyl)ethyl)amine. *Polyhedron* **2012**, *31*, 601−606.
(71) Massoud, S. S.; Louka, F. R.; David, R. N.; Dartez, M. J.; Nguyn, Q. L.; Labry, N. J.; Fischer, R. C.; Mautner, F. A. Five-coordinate metal(II) complexes based pyrazolyl ligands. *Polyhedron* **2015**, *90*, 258−265.
(72) Adach, A.; Daszkiewicz, M.; Barszcz, B. Experimental and theoretical studies on the structure and spectroscopic properties of N-scorpionate complexes obtained from metallic cobalt in a one pot synthesis. *Polyhedron* **2015**, *95*, 60−68.
(73) Neese, F. The ORCA program system, Wiley Interdiscip. *Rev. Comput. Mol. Sci.* **2012**, *2*, 73.
(74) Neese, F. *ORCA − An Ab Initio, Density Functional and Semi-Empirical Program Package*, Version 3.0.3.
(75) Atanasov, M.; Ganyushin, D.; Pantazis, D. A.; Sivalingam, K.; Neese, F. Detailed Ab Initio First-Principles Study of the Magnetic Anisotropy in a Family of Trigonal Pyramidal Iron(II) Pyrrolide Complexes. *Inorg. Chem.* **2011**, *50*, 7460−7477.
(76) Angeli, C.; Borini, S.; Cestari, M.; Cimiraglia, R. A quasidegenerate formulation of the second order n -electron valence state perturbation theory approach. *J. Chem. Phys.* **2004**, *121*, 4043−4049.
(77) Angeli, C.; Cimiraglia, R.; Evangelisti, S.; Leininger, T.; Malrieu, J.-P. Introduction of n-electron valence states for multi-reference perturbation theory. *J. Chem. Phys.* **2001**, *114*, 10252−10264.
(78) Angeli, C.; Cimiraglia, R.; Malrieu, J.-P. n-electron valence state perturbation theory: A spinless formulation and an efficient implementation of the strongly contracted and of the partially contracted variants. *J. Chem. Phys.* **2002**, *117*, 9138−9153.
(79) Neese, F. Efficient and accurate approximations to the molecular spin-orbit coupling operator and their use in molecular gg-tensor calculations. *J. Chem. Phys.* **2005**, *122*, 034107.
(80) Ganyushin, D.; Neese, F. First-principles calculations of zero-field splitting parameters. *J. Chem. Phys.* **2006**, *125*, 024103.
(81) Neese, F. Calculation of the zero-field splitting tensor on the basis of hybrid density functional and Hartree-Fock theory. *J. Chem. Phys.* **2007**, *127*, 164112−164119.
(82) Rajnák, C.; Titiš, J.; Miklovič, J.; Kostakis, G. E.; Fuhr, O.; Ruben, M.; Boča, R. Five mononuclear pentacoordinate Co(II) complexes as field-induced single molecule magnets. *Polyhedron* **2017**, *126*, 174−183.
(83) Rajnák, C.; Varga, F.; Titiš, J.; Moncol, J.; Boča, R. Field supported single-molecule magnets of $[Co(bzimpy)X_2]$ type. *Eur. J. Inorg. Chem.* **2017**, *2017*, 1915−1922.
(84) Rajnák, C.; Titiš, J.; Moncol, J.; Renz, F.; Boča, R. Field supported slow magnetic relaxation in hexacoordinate Co(II) complexes with easy plane anisotropy. *Eur. J. Inorg. Chem.* **2017**, *2017*, 1520−1525.
(85) Varga, F.; Rajnák, C.; Titiš, J.; Moncol, J.; Boča, R. Slow magnetic relaxation in Co(II) octahedral-tetrahedral system formed of $[CoL_3]^{2+}$ core with bis(diphenylphosphanoxido)methane and tetrahedral $[CoBr_4]^{2-}$ counter anion. *Dalton Trans* **2017**, *46*, 4148−4151.
(86) Smolko, L.; Černák, J.; Kuchár, J.; Rajnák, C.; Titiš, J.; Boča, R. Field-Induced Slow Magnetic Relaxation in Mononuclear Tetracoordinate Co(II) Complexes Containing a Neocuproine Ligand. *Eur. J. Inorg. Chem.* **2017**, *2017*, 3080−3086.
(87) Buvaylo, E. A.; Kokozay, V. N.; Vassilyeva, O. Y.; Skelton, B. W.; Ozarowski, A.; Titiš, J.; Vranovičová, B.; Boča, R. Field-Assisted Slow Magnetic Relaxation in a Six-Coordinate Co(II)-Co(III) Complex with Large Positive Anisotropy. *Inorg. Chem.* **2017**, *56*, 6999−7009.
(88) Valigura, D.; Rajnák, C.; Moncol, J.; Titiš, J.; Boča, R. A mononuclear Co(II) complex formed of pyridinedimethanol with manifold slow relaxation channels. *Dalton Trans* **2017**, *46*, 10950−10956.
(89) Mandal, S.; Mondal, S.; Rajnák, C.; Titiš, J.; Boča, R.; Mohanta, S. Syntheses, crystal structures and magnetic properties of two mixed-valence Co(III)Co(II) compounds derived from Schiff base ligands: Field supported single-ion-magnet behaviour with easy plane anisotropy. *Dalton Trans* **2017**, *46*, 13135−13144.
(90) Rajnák, C.; Packová, A.; Titiš, J.; Miklovič, J.; Moncol, J.; Boča, R. A tetracoordinate Co(II) single molecule magnet based on triphenylphosphine and isothiocyanato group. *Polyhedron* **2016**, *110*, 85−92.
(91) Smolko, L.; Černák, J.; Dušek, M.; Titiš, J.; Boča, R. Tetracoordinate Co(II) Complexes Containing Bathocuproine and Single Molecule Magnetism. *New J. Chem.* **2016**, *40*, 6593−6598.
(92) Woods, T. J.; Ballesteros-Rivas, M. F.; Gómez-Coca, S.; Ruiz, E.; Dunbar, K. R. Relaxation Dynamics of Identical Trigonal Bipyramidal Cobalt Molecules with Different Local Symmetries and Packing Arrangements: Magnetostructural Correlations and ab inito Calculations. *J. Am. Chem. Soc.* **2016**, *138*, 16407−16416.
(93) Nemec, I.; Herchel, R.; Trávníček, Z. Ferromagnetic coupling mediated by Co···$\pi$ non-covalent contacts in a pentacoordinate Co(II) compound showing field-induced slow relaxation of magnetization. *Dalton Trans* **2016**, *45*, 12479−12482.
(94) Habib, F.; Korobkov, I.; Murugesu, M. Exposing the intermolecular nature of the second relaxation pathway in a mononuclear cobalt(II) single-molecule magnet with positive anisotropy. *Dalton Trans* **2015**, *44*, 6368−6373.
(95) Herchel, R.; Váhovská, L.; Potočňák, I.; Trávníček, Z. Slow magnetic relaxation in octahedral cobalt(II) field-induced single-ion magnet with positive axial and large rhombic anisotropy. *Inorg. Chem.* **2014**, *53*, 5896−5898.
(96) Liu, J.-J.; Meng, Y.-S.; Hlavička, I.; Orlita, M.; Jiang, S.-D.; Wang, B.-W.; Gao, S. Determination of zero-field splitting in $Co^{2+}$ halide complexes with magnetic and far-IR measurements. *Dalton Trans* **2017**, *46*, 7408−7411.



DOI: 10.1021/acs.inorgchem.8b01906
*Inorg. Chem.* 2018, 57, 12740−12755